A layered Li-Mn-O based cathode material for lithium-ion batteries with stabilized oxygen redox

Zhansaule Bagindyk, BSc in Chemistry

Submitted in fulfillment of the requirements
for the degree of Master of Science in
Chemical and Materials Engineering

School of Engineering and Digital Sciences
Department of Chemical and Materials Engineering
Nazarbayev University

53 Kabanbay Batyr Avenue,
Astana, Kazakhstan, 010000

Supervisors: Dr. Aishuak Konarov
Dr. Nurzhan Umirov

26.04.2024

DECLARATION

I hereby declare that this manuscript, entitled "*A layered Li-Mn-O based cathode material for lithium-ion batteries with stabilized oxygen redox*", is the result of my own work except for quotations and citations which have been duly acknowledged.
I also declare that, to the best of my knowledge and belief, it has not been previously or concurrently submitted, in whole or in part, for any other degree or diploma at Nazarbayev University or any other national or international institution.

Name: Zhansaule Bagindyk
Date: 26.04.2024

Abstract

The primary cause of the recent, more severe improvement in the global energy problem is the sharp increase in energy consumption. The source of Li ions in the modern lithium-ion battery is the active material in the cathode, which also controls the battery's cost and energy density. Thus, the creation of cathode materials with improved electrochemical characteristics that can replace traditional cathode materials is essential to the evolution of lithium-ion batteries of the future. High-energy chemistry batteries are achieved via the grouping of cationic and anionic activities found in Li-rich materials, which overcomes the conventional capacity limit. Lately, the observed enhanced capacity in relevant systems has been attributed to the anionic electrochemical process associated with oxygen. Nevertheless, using anionic redox reactions unavoidably from the lattice hastens structural deformation and electrochemical performance degradation. Understanding their electrochemical properties becomes crucial to addressing these issues, and it is anticipated that this knowledge will provide helpful advice for the creation of both materials and cells.

Due to Li-rich cathode materials' ability to produce reversing capacities of 200 mAh/g, $Li_2Mn_3O_7$ is a promising source of cathodes for Li-ion batteries. For this work, $Li_2Mn_3O_7$ was synthesized using different precursors (Mn^{2+}, Mn^{3+}, and Mn^{4+} salts and oxides) and characterized by physicochemical and electrochemical methods. The electrodes used in tests were newly prepared and had undergone cycles between 4.8 and 2.0 V vs. Li^+/Li to evaluate their electrochemical properties. Among the $Li_2Mn_3O_7$-0 (LRM0), $Li_2Mn_3O_7$-1 (LRM1), $Li_2Mn_3O_7$-2 (LRM2), and $Li_2Mn_3O_7$-3 (LRM3), the LRM0 showed higher specific capacity of 216 mAh/g with retained capacity of 74.8% after 50 cycles. Besides, LRM1 delivered the lowest capacity but highest capacity retention of 89% over 50 cycles. From electrochemical and characterization tests, the difference in performance of materials related to starting materials was identified, leading to the need for further studies. Considering the same synthesis condition and final chemical composition, the obtained results distinguished in cationic and anionic redox reactions.

Acknowledgments

I would like to thank my supervisors, Prof. Aishuak Konarov and Dr. Nurzhan Umirov, for all their support and insight throughout the thesis writing process. The assistance I received from Prof. Konarov during my research encouraged me to continue my studies and kept my motivation high.

I am grateful to my seniors and colleagues at NU for their support and care during these two years.

Table of contents

List of Abbreviations

LRM(s)	Li-rich cathode material(s)
LIB	Lithium-ion battery
V	Voltage
TGA	Thermogravimetric analysis
XRD	X-ray diffraction
ssNMR	Solid-state nuclear magnetic resonance
BET	Brunauer-Emmett-Teller analysis
AM	Alkali metal
TEM	Transmission electron microscopy
EIS	Electrochemical Impedance spectroscopy
ICP-OES	Inductively coupled plasma-optical emission spectroscopy
TM	Transition metal
SEM	Scanning electron microscopy
XAS	X-ray absorption spectroscopy
EDS	Energy-Dispersive X-ray spectroscopy
DFT	Density-functional theory
ICE	Initial Coulombic efficiency
XANES	X-ray absorption near edge structure
OCV	Open circuit voltage

List of Tables and Figures

Chapter 1. Introduction

In recent years, energy consumption has significantly increased, and the concern related to energy sources has risen respectively. For the purpose of solving such an issue, a new generation of secondary batteries was presented. Second-generation lithium-ion batteries are rechargeable and have various advantages, namely, high energy density, a broad range of temperature operation, long cycle life, and no memory effect (Zubi et al., 2018). Lithium-ion batteries have an energy density almost twice as high as Ni-Cd batteries when charged at a high voltage. When compared to other systems that use aqueous electrolytes, which typically restrict using voltages to 2 V, LIBs with their higher energy density and employ of nonaqueous electrolytes yield greater operating voltages of 4 V. They also have better intrinsic safety level and have been shown to have excellent cycle life (Zubi et al., 2018; Kim et al., 2023). Lithium-ion batteries with such benefits have become dominant in different fields.

Firstly, understanding the principle of operation of lithium-ion batteries is crucial to examine their safety. A Li-ion battery cell forms of four essential parts, namely cathode, anode, electrolyte, and separator. Negative terminal anodes and positive cathodes are the particles carrying electrons that contribute to the energy storage and release of lithium-ion batteries. The separators provide a fence between the negative and positive ions to prevent the exchange of lithium ions from one side to another (Dunn et al., 2011). During charging, lithium ions go across the electrolyte from the cathode to the anode, and they return back to the cathode during discharge. Since the Li^+ donator in the cathode is the primary key for cell properties, modern commercial batteries get their names from this component. Lithium manganese oxides such as lithium nickel manganese cobalt oxide, lithium cobalt oxide, and so on are utilized as cathode materials (Kim et al., 2023). Due to the capacity mismatch between the anode and cathode materials in the existing energy systems, the development of LIBs has been significantly hampered.

Lithium-ion batteries are used in everything from small appliances like mobile phones to emergency distributed power supplies, electric vehicles, etc. More importantly, LIBs are making inroads to the stock for electric automobiles and are being actively pursued for energy storage on the grid (Manthiram, 2017). A few factors must be taken into account while using lithium-ion batteries in various applications, such as safety, ecological impact, cost, and charge-discharge rate (Yuan et al., 2023). Even though battery research has expanded significantly over the years, its

goals have not changed: ensuring safety, minimizing costs, and shrinking the size and weight of batteries are the goals shared by all battery researchers.

The materials used for the cathode significantly impact how well lithium-ion batteries work. The positive charged material and carbonaceous negative charged materials, into which the Li ion is reversibly inserted and extracted, work together to provide a voltage of more than 3.2 V in the LIBs. The capacity and voltage of the product control the cell's energy density. Therefore, high energy density batteries can be produced for high voltage and capacity material (Manthiram, 2017). In particular, when the same material for the anode is employed, the battery's energy increases, increasing the cathode's potential and material capacity. However, the cathode side, which often exhibits lower specific capacity than anodes, is associated as the issue limiting improvements to the battery's energy density (Yuan et al., 2023). Cathodes of LIBs have a limit on the amount of energy they can store. These electrodes usually function by deintercalating Li^+ during charging and reintroducing it during discharging, while transition-metal ions' oxidation and reduction preserve the charge balance. If the oxygen ions and transition metal ions could both participate in redox processes and store electrons, the cathodes would be able to store energy far more effectively (Kim et al., 2023). To lessen the disparity in capacity between cathode and anode materials, a lot of work has gone into developing next-generation cathode materials with improved electrochemical characteristics. Owing to their notable specific capacity compared to traditional cathode materials, Li-rich cathode materials are thought to be the best choice for new-generation rechargeable lithium-ion batteries. LRM cathodes additionally offer the advantages of being inexpensive, environmentally friendly, and having excellent thermal stability. They also lessen the need for costly and toxic Co. The low initial Coulombic efficiency (ICE), low rate capacity, and severe voltage fading of LRM cathode materials prevent them from being used in more practical applications (Kim et al., 2023). Immediately resolving range and safety concerns is necessary to eliminate them from the electric consumption stock. In this instance, significant advancement has been achieved in the electrochemical reactions of anions, the evolution of positive charged materials structures and their diverse reaction mechanisms during long-time cycles, and other areas.

In this work, $Li_2Mn_3O_7$ was created by implanting intrinsic vacancies from $Na_2Mn_3O_7$ and synthesizing them using different precursors with the same synthesis procedure. Electrochemical tests and characterization methods were conducted to determine the influence of starting materials

on the final product. The primary goal of the research is to achieve greater discharge capacity and good capacity retention and compare the effect of starting materials.

This master thesis consists of five sections. The first section provides a brief introduction and the research goal. The second section reviews the literature on Li-rich cathode materials, particularly their structure, working mechanism, and problems. The section that follows describes the materials and methods utilized in the experiments. The schematic illustrations of implied methods are presented in this chapter. The fourth chapter is focused on the results obtained and future plans. The last section provides a conclusion for this work.

Chapter 2. Literature Review

2.1. Structure of LRM Cathode Materials

Understanding the structure of LRM cathode materials is essential since it significantly affects the process and performance of their electrochemical reactions. Croy et al. (2015) stated that when it comes to phase structure, LMRs are typically thought of as either a solid or a nanoscale mixture made up of layered $LiMO_2$ and layered Li_2MnO_3, which are both equivalent to the layered "α-$NaFeO_2$-type rock salt" structure. Crystalline arrangement representations of $LiMO_2$ and Li_2MnO_3 is displayed in Figure 1. $LiMO_2$ (where M might be metals like Ni, Co, Mn, etc.) typically has a space group of R-3m and a hexagonal layered structure. Furthermore, Li_2MnO_3 is a member of the monoclinic crystal system, having a C2/m space class (Lu et al., 2002). Because these two structures are so similar, it can be challenging to discern between them, making understanding the LRM structure extremely hard. Also, they exhibit tightly packed cubic oxygen arrays, with AM and TM occupying all octahedral positions. The primary diffraction patterns of LMRs can be found to align well with the R-3m depending on their XRD data (Qing et al., 2015). LRMs require more sophisticated characterization methods to comprehend their original phase structure in addition to the XRD results.

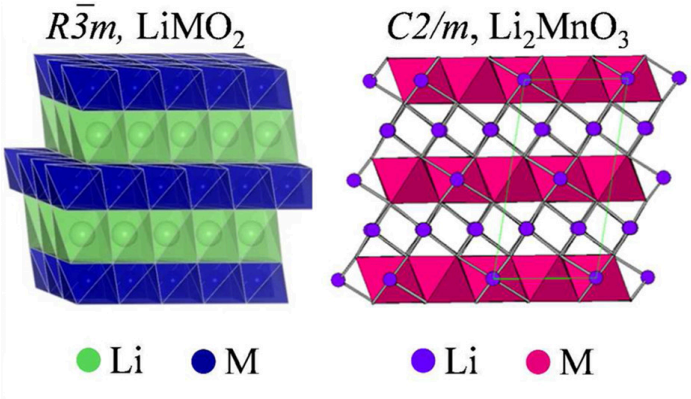

Figure 1. Crystal structure illustration of $LiMO_2$ and Li_2MnO_3. From "Review of the U.S. Department of Energy's "Deep Dive" Effort to Understand Voltage Fade in Li- and Mn-Rich Cathodes," by Croy et al., 2015, Accounts of Chemical Research, 48(11), p. 2813–2821.

2.2. LRM cathode material reaction mechanisms

The charge-discharge reaction mechanism of the first and second cycle are the two main reaction processes of the LRM cathode materials. The initial charge-discharge reaction process has numerous contradictions because of the complex reaction mechanisms of LRM. After conducting in situ XRD and examining obtained data, Lu et al. (2003) hypothesized oxygen loss theory. The authors proposed that the elimination of excess Li ions and oxygen release in the first charge were the sources of the irreversible plateau at 4.5 V. In opposition to the theory of Lu et al. (2003), Robertson and Bruce (2003), in the same year, developed a hypothesis for the exchange of Li ions with H^+. In their work, pristine, charged, and discharged Li_2MnO_3 electrodes without any exposure to air were studied in TGA/MS analysis. The derived results of H_2O loss were as follows: ≥1%, 10.699%, and 5.309% of the active material, respectively. Furthermore, ssNMR results verified that protons were present in the sample in the final charging phase. Robertson & Bruce (2003) explained their hypothesis that the electrode, during the charging process, hydrogen ions formed at the electrode surface consequently. After formation, these ions were exchanged with Li ions in the electrode. H^+ ejection is a possible outcome of the oxidation of the carbonyl group in electrolytes as they were reactive at voltages higher than 4.4-4.5V (Lu et al., 2003). H^+ is extracted and replaced by Li^+ upon discharge due to electrochemical reduction in non-aqueous electrolytes (Robertson & Bruce, 2003). Creating a positive electrode with charge compensation at the TM site during deintercalation of lithium ions is one major approach to increase the specific energy of batteries.

Temperature plays a role in both of the compatible mechanisms discussed above. Armstrong et al. (2005) stated that at 30°C, oxygen loss predominated, while at an approximately twice higher temperature, the H^+ exchange process dominated. In particular, they discussed that when O loss is predominant, this is explained by O loss at the outer layer of the particle and O diffusion of the cations within the particle's center, taking up positions that Li initially held rather than O diffusion in the lattice. Thackeray et al. (2007) developed a phase diagram (Figure 2) to demonstrate LRM's multistep reaction process. This Figure 2 depicts the initial cycle graph of "$x$$Li_2MnO_3 \cdot (1 - x)LiMO_2$ (x=0.3)". The oxidation of TM ions and the elimination of Li^+ ions from alkali metal slabs are the primary causes of the capacity increase at voltages <4.4 V in the first charging curve. This ultimately results in the creation of TMO_2 from $LiTMO_2$. In the meantime, the structure will be supplemented and stabilized by alkali metal ions from Li_2MnO_3

diffusing into the lithium depletion. The long plateau at voltages >4.4V, as explained by Thackeray et al. (2007), came from Li ions extraction and oxygen release, which encouraged the converging of Li_2MnO_3 to manganese dioxide. Hy et al. (2014) provided direct proof of Li_2O production using in situ surface-enhanced Raman Spectroscopy (SERS). This analysis was conducted to investigate the oxygen-related surface responses during charge discharge. The subsequent discharge resulted in an irreversible loss of capacity since MnO_2 can only be converted into $LiMnO_2$, whilst TMO_2 can be converted to $LiTMO_2$ (Trackerey et al., 2007). Less is known about the aforementioned reaction mechanism, including how lattice oxygen evolved and where high specific capacity came from, as study on the LRM positive charged materials' reaction mechanism has progressed.

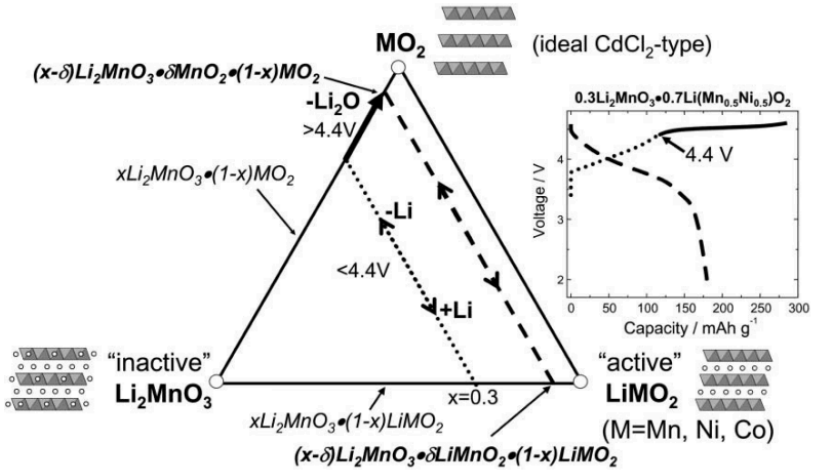

Figure 2. Structural phase schematic for an $xLi_2MnO_3 \cdot (1 - x)LiMO_2$ electrode, illustrating the electrochemical reaction paths. From "Li_2MnO_3-stabilized $LiMO_2$ (M = Mn, Ni, Co) electrodes for lithium-ion batteries," by Thackeray et al., 2007, Journal of Materials Chemistry, 17(30), p. 3112.

Various methods were employed to understand better chemistry of Li-rich cathode materials. Jiang et al. (2009) employed ex-situ characterization methods to identify the gasses coming from the cells. They indicated that electrolyte breakdown may have contributed to certain portions of the oxygen loss but not oxygen release, as no O_2 was discovered during ex-situ analysis (Jiang et al., 2009). Additionally, their material $Li[Li_{1/9}Ni_{1/3}Mn_{5/9}]O_2$ showed better cycling performance at high voltage windows of 5.3-2.5V rather than at 4.6-2.5V (Jiang et al., 2009). Other authors determined oxygen extraction from the lattice and CO_2 at higher voltages

via operando mass spectroscopy (Luo et al., 2016). Luo et al. (2016) used a variety of spectroscopic methods to show that the main mechanism for charge adjustment is the formation of holes (electrons) on oxygen atoms that are coordinated with TM and alkali metal ions through moderately ionic interactions. They carried out Raman spectroscopy and compared peaks of their material and compounds containing O_2, but they did not detect evidence indicating the presence of O_2. Lithium deintercalation causes the host structure to become denser and lose oxygen within the surface (Koga et al., 2013). However, densification involves the transfer of transition metal ions out of the particle's outside towards its center becomes increasingly challenging, maintaining the pristine structure across most particles. As a result, partial oxygen oxidation caused by the rise in Mn-O bond covalence brought on by the abundance of vacancies of lithium in the transition metal layers takes place within the opposite direction of the surface (Koga et al., 2013). Overall, Koga et al. (2013) concluded that oxygen is electrochemically active in the presence of many lithium vacancies interacting with MnO_6. Thus, it is essential to understand the working process of LRM positive charged materials.

The mechanism of "reversible oxygen redox reaction" and the concept of oxidation of manganese are the two primary theories that attempt to interpret the genesis of greater specific capacity. The mechanism of the reversing oxygen redox reaction pertains to the reversing transition of divalent O^{2-} and its higher valence, like O^{-}, which serves as a capacity contributor throughout the cycles (Koga et al., 2014). McCalla et al. (2015) detected oxygen-oxygen pairs lying between Ir atoms by TEM image. They clarified that their material (Li_2IrO_3) took the O1 structure at a charged state, thus enabling them to observe the formation of O-O pairs via TEM in a way that prevents the oxygen columns' projection from intersecting the metal slabs. Li et al. (2018) investigated $Li_{1.2}Ni_{0.2}Mn_{0.6}O_2$ during initial charge-discharge cycles and presented solid evidence of the development of peroxo-like oxygen bonds. They performed in situ Raman spectroscopy and XRD, where 003 peak shifts were illustrated, as well as the appearance of O-O pairs. In fact, Li^+ removal from the alkali metal layers is followed by an increase in attraction between oxygen protons and electrons, which causes the unit cell to become more extendible along the c-axis and shift 003 towards lower degrees. Following this process, Li ions get removed from the TM slabs, allowing the unit cell to alter inversely and shift 003 upward to greater reflection angles (Li et al., 2018). A peroxo-like oxygen stretch region was detected at around 850 cm^{-1}, which is within the common area (700-900 cm^{-1}) and rises at higher voltages, and fades

away in the following discharge process. It should be noted that due to different thermodynamic circumstances resulting in diverse environments (neighboring atoms) around oxygen atoms, the potential for the appearance of O-O pairs would be varied in other systems (Sathiya et al., 2014). Also, the above-mentioned oxygen stretch region was repeatedly observed in the second cycle. Moreover, a theory concerning the formation of a peroxo-like bond along the c-axis is proposed by combining the variable tendency of the c-axis width shown in XRD findings with the variations in O-O pair dimension reported in Raman data (Li et al., 2018). The authors further supported this theory by DFT calculations. Alternatively, some authors proposed alternative mechanisms to explain the excess capacity of LRM cathodes, particularly the oxidation of Mn from +4 to +7 (Radin et al., 2019; Thackeray M., 1997; Fischer et al., 1993). Radin et al. (2019) claimed that the oxidation of Mn goes along with the movement to tetrahedral from octahedral sites, resulting in the plateau of high voltage in the initial cycle. However, the authors emphasize the difficulty of experimentally verifying such an assumption because oxides containing Mn +7 can easily break. The above-mentioned hypotheses are presently in the early phases of development and have certain shortcomings. Indeed, the concept of the reversible oxygen redox reaction is commonly acknowledged. Still, many problems need to be solved, like oxygen redox activity activation techniques and so on.

Seo et al. (2016) examined the charge/spin density and density of state around oxygen ions in diverse neighborhood conditions by applying computational mechanical modeling (DFT). The results show how the local environment and excess Li rate affect oxygen redox activity. Furthermore, oxygen ions align with the closest TM x 2 and Li x 4 ions when excessive Li is present, generating Lithium-Oxygen–Transition Metal and Lithium-Oxygen–Lithium combinations. Unlike the O 2p bands in the Li–O–TM combination, the O 2p bands in the Li–O–Li arrangement are unable to create a hybridized orbital because of the significant energy differential between AM and anion orbitals. Because of this trend, the O 2p orbital within the Li-O-Li structure has to expand. At elevated charging voltages, it autonomously stretches across energy bands and starts to supply electrons. This is when oxygen redox starts (Seo et al., 2016). If there is a considerable difference in the ionic radii of AM and TM, the detrimental TM migration would be inhibited. Regarding this, compounds containing lithium and sodium appear promising, and their ionic radii contrast more with those of 3D TMs.

The redox pair development and structural change need to be given consideration when assessing the electrochemical capabilities during cycling. In order to study the redox couple evolution, Hu et al. (2018) conducted ex-situ and in-situ studies of $Li_{1.2}Ni_{0.15}Co_{0.1}Mn_{0.55}O_2$. From the electrochemistry of the material, voltage fade was clearly seen upon cycles. In addition to this, XAS results showed an alternation of spectra of TMs within the first, second, twenty-fifth, forty-sixth, and eighty-third cycles. Accordingly, Hu et al. (2018) emphasized the reduction of valence states of TMs with an increase in charge-discharge cycles affected by oxygen loss. Further, pre-edge peak intensity continuously diminished during testing, suggesting a lowering bonding strength between the TM and bulk oxygen. Interestingly enough, the contribution to the capacity of nickel and oxygen gradually decreased, while the capability of manganese and cobalt increased in the subsequent cycles (Hu et al., 2018). The above-mentioned diminished bonding between bulk oxygen and TM results in the reduction of oxygen capacity contribution.

Apart from redox pair evolution, the phase shift of LRM from layered to spinel phase is one of the issues causing insufficient rate performance along with fading. Nevertheless, where the spinel phase forms and how it develops after consuming the layered structured phase remains unclear. To open up the mechanism beyond the structure transformation, Xu et al. (2011) stated the displacement of TM ions onto Li slabs might trigger the creation of spinel close to the particle surface. Alongside the change of state, Li^+ and O^{2-} removal accompanied, causing significant lattice strain and crack formation. After cycling, certain stacked nanoparticles also showed signs of cracks and pores, which are thought to be the result of lattice breakage and vacancy formation following the elimination of lithium ions (Gu et al., 2013). After 100 prolonged cycles, large spinel grains were found in the $Li_{1.2}Ni_{0.13}Co_{0.13}Mn_{0.54}O_2$ system near the surface, initiating phase transition along with “defect domains” (Liu et al., 2018). Furthermore, Yin et al. (2020) examined the structure evolution under an expanded potential window during the initial cycle and put forth an alternative morphological evolution mechanism. The authors indicated that, firstly, Co^{3+} and Ni^{2+} oxidized, following anions oxidation and migration of Mn until the charge reached 4.6V. Li^+ were progressively evacuated to the completely unlithiated state alongside the oxygen evolution once the voltage rose to highest voltage (4.8V), and TM^+ filled the cationic deficiencies. Based on the obtained operando XRD data, the formation of bulk A’ phase and disordered rocksalt-spinel layer during charging were detected. In the subsequent discharge, only a portion of the transported cations can return. There are still disagreements on the reaction mechanism of Li-rich

cathode materials at several crucial places, which must be resolved individually before a comprehensive theory that can explain more phenomena and direct future research can be developed.

2.3. Challenges Li-rich cathode materials encounter

Since their first introduction, LRM cathode materials have faced numerous issues relating to the material and the battery system. In particular, great capacity reduction in the first charge-discharge cycles, not sufficient rate performance, and capacity fading upon cycles. Unlike other materials, LRMs show lower Initial Coulombic Efficiency (ICE) owing to their individual initial cycle mechanism. Importantly, LRMs possess a plateau at 4.5V, appearing due to the Li ions being extracted from the lattice. There are two main phases of LRMs: R-3m rhombohedral layered, contributing to the capacity lower 4.5V, and C2/m Li-rich phases, providing the capacity at higher voltages. It is possible to categorize Li_2MnO_3 and $LiTMO_2$ as layered α-$NaFeO_2$-type rock-salt formations as they have occupied all eight octahedral positions in their oxygen arrays (Wang et al., 2016).

The major advantage of LRMs is the extraordinarily great specific capacity (≥250 mAh/g); yet, the former consistently show a constant voltage fade after extended repeated cycles, challenging their commercialization. Different studies were conducted to shed light on the mechanism behind voltage fade. Further, it has been noted that the way lattice oxygen behaves over extended cycles significantly impacts voltage degradation. The monoclinic phase of Li_2MnO_3 is permanently activated at charges greater than 4.5 V. The oxygen loses electrons and changes from O^{2-} to O^- or O_2 balances the negative valence resulting from Li^+ delithiation (Hu et al., 2018). Such reactions lead to TM ions reduction. Following oxygen loss, oxygen vacancies are created, which reduce the strength of the O and TM bond, facilitating structure changes and TM shift (Gent et al., 2017). Seteni et al. (2017) suggested that a small peak around 2.7-2.8V was associated with Mn reduction from 4+ valence to 3+, analyzing dQ/dV curves of $Li_{1.2}Mn_{0.54}Ni_{0.13}Co_{0.13}O_2$. Moreover, Hu et al.'s research (2018) verified that oxygen evolution causes a constant decrease in the average valence state of TMs. XANES data provided strong evidence showing the reduction of all TMs present in the sample. Hu et al. (2018) defined OCV as "The open-circuit voltage (OCV) in LIBs is determined by the relative Fermi level with respect to the Li^+/Li^0 energy level". On the other hand, when engaged oxygen levels are lowered, the

Mn^{3+}/Mn^{4+} and Co^{2+}/Co^{3+} redox sets are activated. This raises the Fermi level, lowers OCV and operating voltages, and ultimately causes voltage decay. Not only due to TM reduction but also capacity loss occurs when the TM-O covalency weakens, resulting in reduced oxygen involvement in the redox processes and a drop in the oxygen species capacity contribution.

Changes that happen during cycling, such as the production of oxygen vacancies and weakened bindings between TMs and O, facilitate phase transformation. Xu et al. (2011) found a decrease in Mn-O bond strength accompanied by a lowered Mn oxidation state using the Electron Energy Loss Spectroscopy. Additionally, they made a comparison between post-cycling and pristine LRM samples and hypothesized that after 10 cycles, electrode particle surfaces would exhibit distinct spinel patterns. The suggestion was made from the absence of these structures in the pristine sample, which implied surface changes during charging. Given these points, the evolution of O during extended cycles creates disorganized-directed spinel structures, which in turn causes structural deterioration and voltage drop. Nevertheless, it is yet unknown how ions migrate during the phase transition.

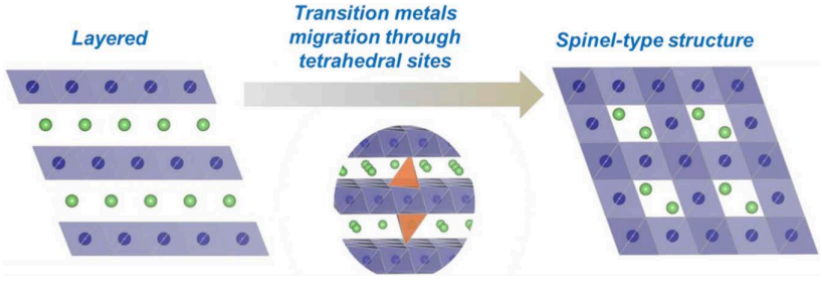

Figure 3. Diagram showing the phase change from layered to spinel-type structure. From "Aluminum and Gallium Substitution into 0.5Li2MnO3·0.5Li(Ni0.375Mn0.375Co0.25)O2 Layered Composite and the Voltage Fade Effect," by Lee et al., 2014, Journal of the Electrochemical Society, 162(3), p. A322–A329.

Lee et al. (2014) attempted to explain ion migration by providing a possible schematic of phase transition (Figure 3). At the time the percentage of Li and O hits a particular amount, TM ions start reorganizing and relocating to Li's tetrahedral sites from their octahedral ones. This process is known as TM migration. According to Lee et al. (2014): "The Li–Li dumbbell structure is formed during this process by the Li^+ ions in the TM layer migrating in the opposite direction towards the face-shared tetrahedral sites." Following the formation of the Li-Li pair, the structure's total energy also decreases because the transition metal ions within the framework

could possibly move similarly to Li. It should be pointed out that such pairs of Li-Li are always present, and Li ions in tetrahedral sites are most likely to build spinel form (Lee et al., 2014). Additionally, Zheng et al. (2015) illustrated a comprehensive phase transition procedure of $Li_{1.2}Ni_{0.2}Mn_{0.6}O_2$. In accordance with the observations indicate that the LRMs experience a shift in phase from a layered to a Fm-3m spinel structure. In brief, the failure to completely preserve layered ordered structure during high charge outputs results in the fading of voltage upon continuous cycles.

Chapter 3. Description of conducted work & research

3.1. Ion-Exchange Method

A novel approach to ion-exchange synthesis has surfaced in recent years, with the goal of attaining significant advancements in material synthesis. Particularly, this method is a chemical reaction associating the elimination of atoms from the structure that serves as the host and its replacement with the desired alkali metal due to similar ionicity and thermodynamic driving force. The structure of the initial substance is maintained by the ion-exchange process. Reaction rates often rise with increasing ion exchange temperature. However, this is accompanied by a rise in imperfections in the lattice of the end-product matter. Thus, in comparison to high-temperature heating, ion exchange at low temperatures is advantageous for the materials' excellent crystal formation and also helps to save energy usage. Also, metastable phases of materials that are not synthesized by solid-state reactions at high temperatures can be obtained via ion exchange (Cao et al., 2021). In addition, the following method for ion substitution reactions occurs between replaceable ions in the ion exchanger and the ions in the solution.

$$A^+X^-(solid) + B^+Y^-(solution) \rightarrow B^+X^-(solid) + A^+Y^-(solution) \quad (1)$$

While the substituted ion dispersed in the ion-exchanger medium from the lattice, at the same time, the desirable cation spread into the latter. Ion exchange is propelled by a variation in chemical potential between both kinds of ions, which allows ions to travel into the crystal structure and achieve a stable product with greater lattice enthalpy. This process mainly involves the exchange of cations, such as Na^+ ions being swapped for Li^+ ions (Figure 4). Using high temperatures can lead to a quick breakdown of the structure. The cation flows more quickly compared to the anion because its radius is less than that of the anion (Chen et al., 2021). Using ex-situ structural studies of $NaNi_{0.5}Mn_{0.5}O_2$ after various chemical exchange periods, Gwon et al. (2014) examined the ion exchange mechanism. The authors discovered that the ion exchange involved multiple intermediary complicated molecules rather than a straightforward two-phase process (Figure 4-c). With incredibly quick exchange kinetics, the transitional phase of the beginning stages of ion exchange arises virtually instantly and comprises randomly dispersed Na^+

and Li^+ in the lithium layers. However, Gwon et al. (2014) emphasized that the mentioned method involving $NaNi_{0.5}Mn_{0.5}O_2$ differs significantly from earlier literature findings that demonstrated two-phase-like activity in the absence of the development of a persistent intermediary period. Also, the authors concluded that slight Na^+ content in the layers may be able to stop the layer space from collapsing, which is frequently seen in materials with distinct layers.

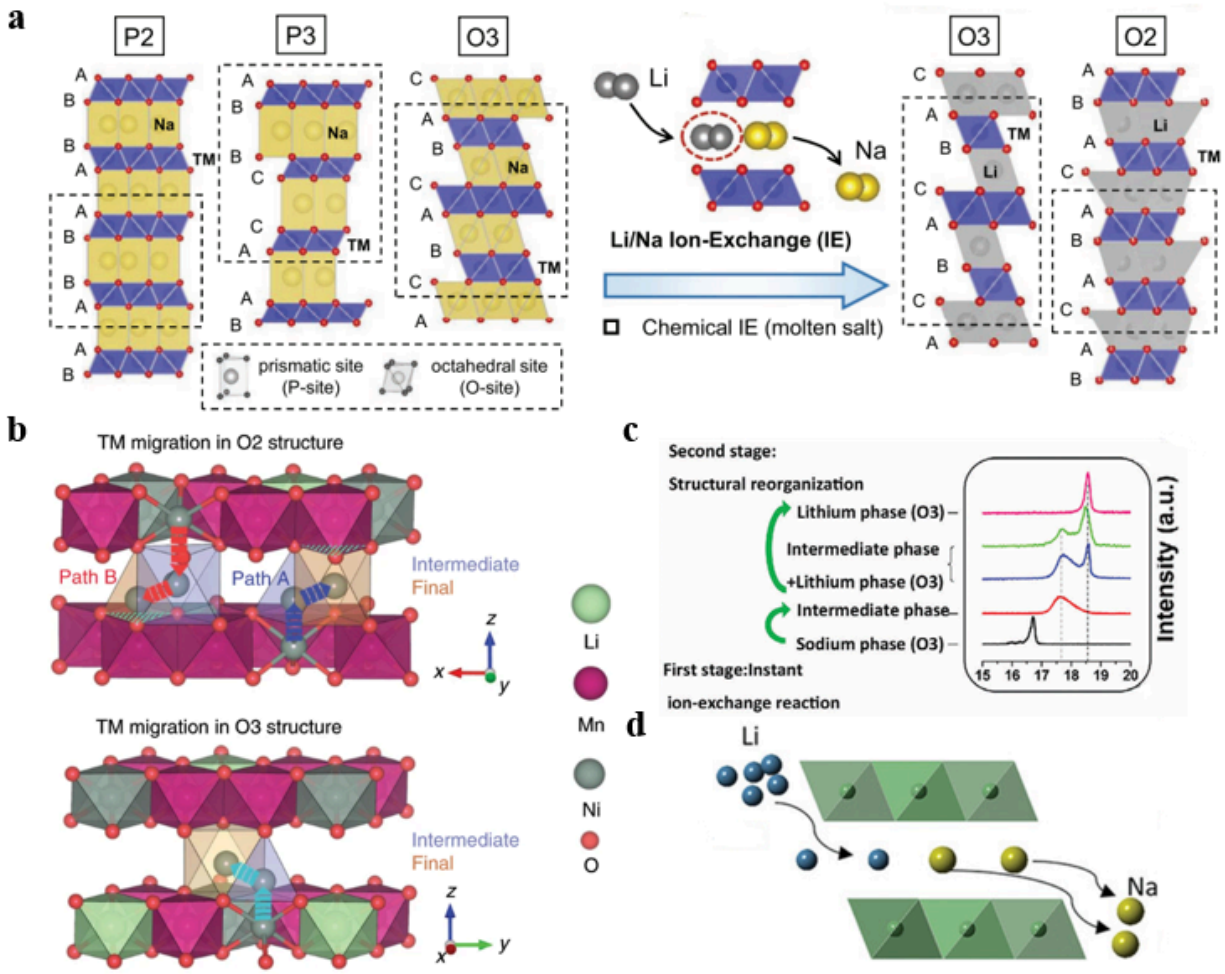

Figure 4. a-d) An overview of the ion-exchange synthesis's mechanisms by Luo et al., 2023; b) Migration routes of TM from the initial to the intermediate and last Li sites by Eum et al., 2020; c) XRD patterns of different phase states by Gwon et al., 2014.

More importantly, Li-ion cathode materials with distinct crystal structures that are often unattainable through solid phase sintering can be accomplished via ion exchange techniques. Although ion-exchange synthesis has evolved significantly, detailed explanations remain unclear and require further theoretical calculations and enhanced characterizations.

3.2. Material Synthesis

$Na_2Mn_3O_7$ as cathode material is derived by conventional solid-state method mixing different types of manganese and sodium salts in accordance with the proper stoichiometric ratio. After the mixture was pelleted, it was calcined in air for five hours at 600 °C. During the heat treatment, the material heated at a rate of 5 °C per minute and cooled naturally to room temperature. $Li_2Mn_3O_7$ was obtained from $Na_2Mn_3O_7$ precursor using the ion-exchange method. $Na_2Mn_3O_7$ and 10-fold excess Li molten salt (88% $LiNO_3$ and 12% LiCl) were mixed and subjected to heat at 280 ◦C for 4 h in the air. Following many washes with distilled water, the mixture was left to dry overnight at 110 ◦C.

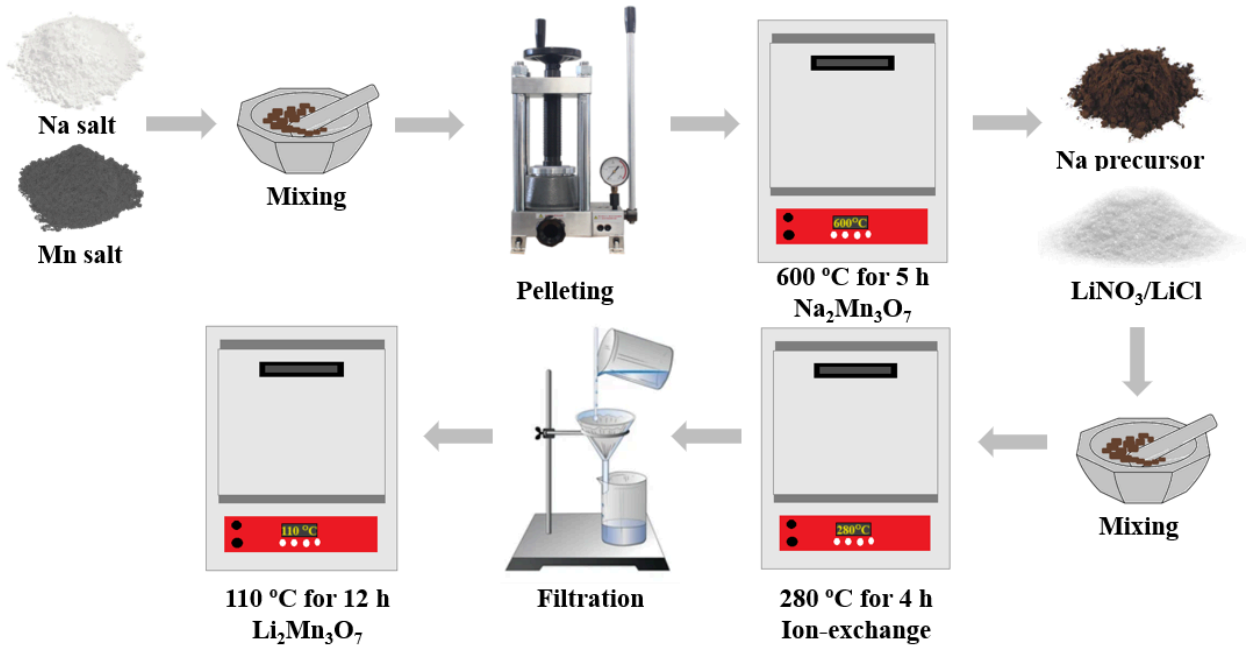

Figure 5. Schematic illustration of the synthesis procedure of $Li_2Mn_3O_7$

By adding an extra heating step after ion exchange, spinel-type $Li_2Mn_3O_7$ was derived. After the above-mentioned synthesis procedure was completed, the sample was repeatedly heated but at 700 ◦C for five hours in the muffle oven. For the purpose of checking the high-temperature effect on the sample. As mentioned, high-temperature heating during ion exchange causes the collapse of the sample's structure.

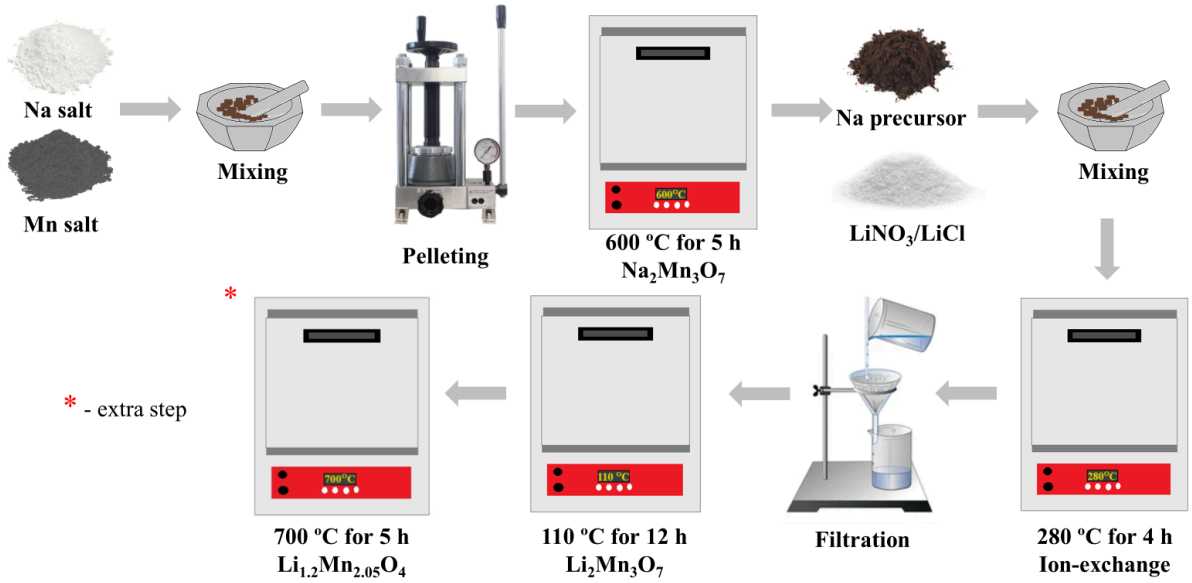

Figure 6. Schematic illustration of the synthesis of spinel $Li_{1.2}Mn_{2.05}O_4$

3.3. Characterization methods

X-ray diffraction (XRD, Rigaku MiniFlex) was utilized to determine the crystal structure of the Na precursor $Na_2Mn_3O_7$ and $Li_2Mn_3O_7$, with a step size of 0.01° and a speed of 7°/min over a 2θ range of 10−80°, operating at 40 kV and 150 mA with a Cu $K\alpha_{1/2}$ (λ=1.5406Å) radiation form. The SEM (ZEISS Crossbeam 540) was used to characterize the form and structure of samples. Once the Na^+/Li^+ ion exchange procedure was completed, the elemental distribution within the particle was determined using scanning electron microscopy (SEM)/EDS (JEOL JSM-IT200). TEM images were taken with JEOL JEM - 1400 Plus. The contents of Li, Na, and Mn were identified by ICP-OES (Thermo Fisher Scientific).

The electrodes for ex-situ XRD were collected by dismantling the cells in several states within a glove box filled with argon. They were then repeatedly cleaned with ethyl methyl carbonate (EMC) and vacuum-dried.

The thermal characteristics of the as-synthesized materials have been explored using differential scanning calorimetry (DSC) and thermogravimetric analysis (TGA). Thermogravimetric analysis (TGA) was performed at 10 ◦C/min under nitrogen flow using a thermal analyzer system (STA 6000, Perkin Elmer). The Brunauer Emmett Teller (BET) surface

area analysis was performed through a Quantachrome Autosorb-iQ3-MP/Kr BET surface analyzer.

A thorough explanation of the Li-ion batteries modified in-situ Raman (The Horiba LabRam Evolution) cell was used. In particular, a viewing window consisting of a thin glass window with a thickness of 0.47 mm is installed on top of the cell. In Figure 7, the design and preparation of the Raman cell are given. The argon-filled glove box was used to assemble the cell. The self-standing electrode was prepared for Raman spectroscopy via blending 70 % active material (LMR0), 20 % carbon black, and 10% poly(tetrafluoroethylene) binder (PTFE) that is soluble in water. Before using a self-standing electrode with a PTFE binder, an electrode with PVDF was analyzed. However, due to challenges related to placing the active material face upward and detecting it with a laser, the choice to try with a self-standing electrode was made. It is important to note that in the case of using PVDF binder, besides putting the active material face upward, a tiny hole was drilled in the middle of the Celgard separator and Li chip to allow the beam of the laser and signals to pass through. On the other hand, utilizing a self-standing electrode with a PTFE binder did not necessitate this kind of handling, and it is a simpler technique to use.

The electrode surface was exposed to the red line of an air-cooled Helium Neon laser with a wavelength of 633 nm. To guarantee that the Raman spectra were reliable and repeatable, at least three separate locations on the electrode's surface were examined. The electrochemical measurements were run using a potentiostat to control the in-situ Raman test (Potentiostat Biologic SP-50e) at room temperature. 50 mA/g of current density was employed for the galvanostatic control. The OCV in the majority of the research instances was over 3.0 V.

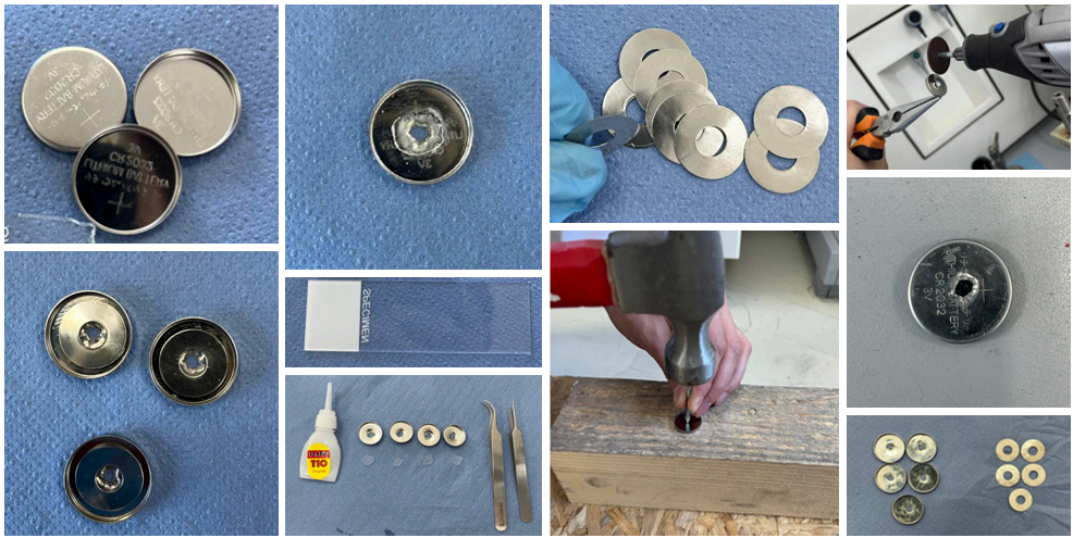

Figure 7. Illustration of preparation of "home-made" cell for Raman Spectroscopy

3.4. Electrochemistry

Coin cells were assembled in order to evaluate the prepared cathode materials' electrochemical performance. 70% active mass, 20% carbon black, and 10% poly(vinylidene fluoride) (PVDF) (Solef, 5130) binder were combined to create the electrodes in N-methyl pyrrolidine (NMP) (Sigma-Aldrich) and coating a slurry on surface of an Al foil current collector. The cathode electrode was punched into a 14 mm circular disc after being dried for 12 hours in a vacuum oven. The average loading of mass of the electrode is around 2 mg. Coin cells of the R2032-type were built using the electrode, Li metal as anode, Celgard separator, and 1 M lithium hexafluorophosphate (LiPF6) dissolved in ethylene carbonate: diethyl carbonate: ethyl methyl carbonate (EC:DEC:EMC) (1:1:1) as an electrolyte in an argon-filled MBraun glovebox. The water and oxygen concentrations were kept to be ≤ 0.1 ppm. Additionally, in the sodium-ion battery assembly, the standard same cell was used, which consisted of the prepared electrode, separator (glassy fiber, Whatman), Na metal served as an anode, and sodium hexafluorophosphate ($NaPF_6$) 0.5 M dissolved in propylene carbonate with 2% fluoroethylene carbonate additive (PC: FEC) mixture (1:1). Using a WonATech battery tester, the galvanostatic charge-discharge cycle tests were run within the voltage range of 2-4.8V. The C rates employed in the rate capacity tests were 0.1C, 0.5C, 1C, 2C, and ultimately 0.1C once again. The cells were tested at a comfortable temperature (~25 °C).

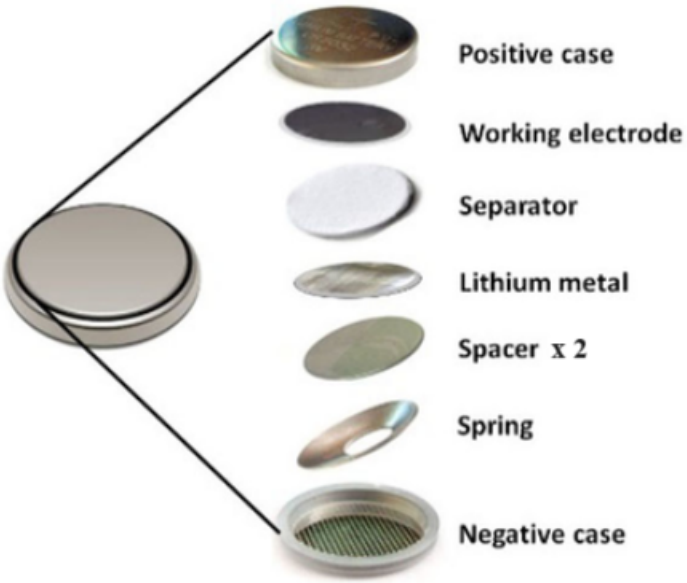

Figure 8. R2032 coin cell configuration design. From "Research on the assembly process of full coin cells: key factors affecting data reliability," by Xue et al., 2023, Ionics, 29(12), p. 5285–5293.

Impedance spectra (EIS) of electrochemical reactions were captured with a Biologic SP-50e workstation. The frequency range covered by was an amplitude of 5 mV and a frequency range of 100 kHz to 0.1 Hz.

Chapter 4. Presentation of results

In order to make it easier to understand, the samples were named as follows:

LMR0 - precursors used: Mn_2O_3+NaOH

LMR1 - precursors used: MnO_2+NaOH

LMR2 - precursors used: $MnCO_3$+NaOH

LMR3 - precursors used: $MnCO_3$+$NaNO_3$

LSP - synthesized by repeatedly heating LMR0: spinel $Li_{1.2}Mn_{2.05}O_4$;

4.1. Characterization methods: Part I

The XRD pattern of the Na-precursor $Na_2Mn_3O_7$ was confirmed as a space group P1, while ICP-OES verified its chemical formula (Figure A.1). Based on the particular location in the AM site, the sodium coordinating environment varies as an octahedral or prismatic, along with the TM layer displaying a vacancy in the Mn ordering pattern (Cao et al., 2022). Furthermore, images from TEM and SEM demonstrate the uneven form of $Na_2Mn_3O_7$, a secondary particle made of parent nanoparticles. The TEM picture displays a crystalline layered structure with a 110 plane-fitting interlayer spacing of about 0.53 nm (Figure B.8) (Cao et al., 2022). Additionally, the electrochemical performance of $Na_2Mn_3O_7$ is listed in the Appendix section (Figure C.1). The graph shows that two reversible plateaus with comparatively little voltage hysteresis emerged at <4.15 V, suggesting that reversing anionic redox activities might be achieved due to the forming of the Na-O-vacancy. Calculations using density functional theory (DFT) were used to verify that O-O 2p orbitals exist in $Na_2Mn_3O_7$ (Benoit et al., 2018). The plateau at 2-2.5V corresponds to a reversible redox of $Mn^{3+/4+}$. The peak at 4.25V is linked to anionic redox reaction. The ion exchange method allows the preservation of the arrangement and layered orientation of the Mn layer, and Na ions may be substituted by Li ions during this process. Therefore, the sample after the ion exchange method is anticipated to maintain its layered structure and TM vacancies of Na-precursor materials.

XRD data outcomes demonstrate that $Li_2Mn_3O_7$ might be classified as an O3-type with a hexagonal R-3m space group. It is observed that diffraction intensity peaks are decreased after ion exchange, which might be due to crystallographic defects occurring when the correct arrangement of stacking planes is broken (Raekelboom et al., 2001). Furthermore, an impurity

can be observed, which is compatible with the ICP data, because of the leftover Na^+ in the alkali metal layer after the ion exchange method (Table 1) (Kim et al., 2023). Also, there are differences in intensity and peaks widths of samples as seen in Figure 9 below. Above that, Rietveld refinement profile (R_{wp} = 6.95%) of lab scale XRD data prove the space group of R-3m O3 phase. The superlattice peaks by arranging the Mn-vacancy distribution in the TM layer at 20-30 2 theta are detected (Cao et al., 2022).

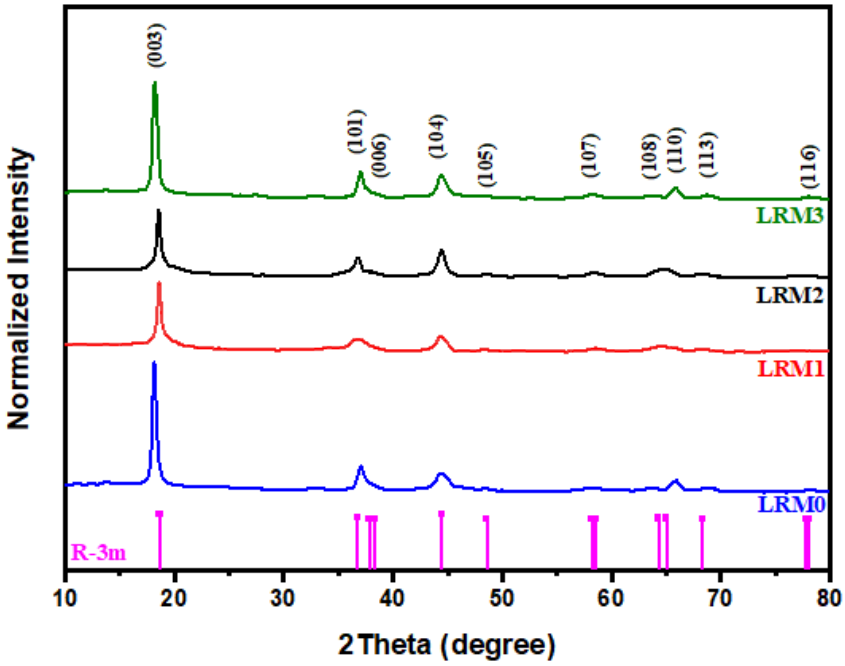

Figure 9a. XRD patterns of LMR0, LMR1, LMR2, and LMR3

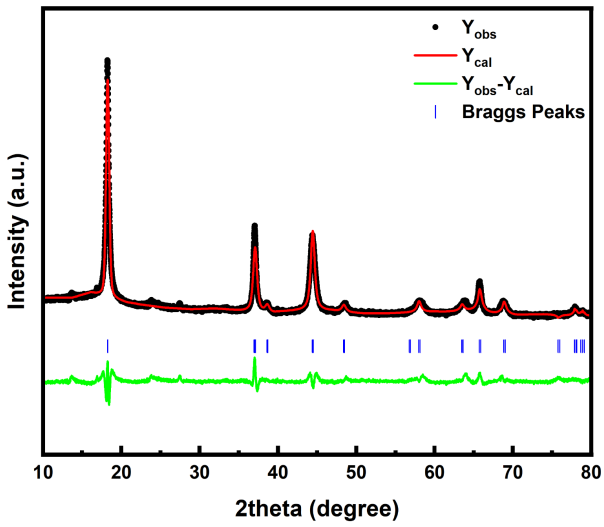

Figure 9b. Rietveld refinement profile of XRD data of as prepared material

Table 1 presents the results of inductively coupled plasma optical emission spectroscopy (ICP-OES) measurements of the chemical composition of $Li_2Mn_3O_7$ and $Na_2Mn_3O_7$. As seen, the molar ratio of each element in all samples, except LRM1, is extremely close to the original formula. It can be concluded that the LRM1 ion exchange method was not successful, and needs to be repeated more than one time.

Table 1. ICP results of before and after ion-exchange samples

Measured atomic ratio			
Sample name	**Na**	**Li**	**Mn**
Blank	0	0	0
$Na_2Mn_3O_7$-0	2.02	0	2.98
LMR0	0.02	1.99	2.95
$Na_2Mn_3O_7$-1	2.07	0	3.17
LMR1	0.37	1.67	3.16
$Na_2Mn_3O_7$-2	2.13	0	2.96
LMR2	0.02	2.14	2.95
$Na_2Mn_3O_7$-3	2.09	0	2.91
LMR3	0.026	2.01	2.89
LSP	0.02	1.25	2.05

The form and structure of the materials was studied. SEM and TEM images illustrate that materials before and after ion exchange show similar morphology, demonstrating the effectiveness of this method for preparing layered LRMs. The SEM images (Figure 10) demonstrate that the material's particle size exhibits similar morphology after ion exchange. LRM1 exhibits larger particle sizes among samples before and after ion exchange. The materials are made up of two different kinds of particles: big ones with shaped edges and little ones with irregular shapes. Better electrochemical performance results from the smaller particle size since it shortens the migration path of Na/Li ions and promotes larger surface area. SEM-EDS mapping of Mn, Na, and O showed a uniform distribution of elements. Unfortunately, EDS cannot detect

Li metal due to its “low energy of characteristic radiation.” Notably, only in LRM1 Na content was detected during EDS analysis (Appendix, Figure B.6). Even though a trace amount of Na is present in all samples as confirmed by ICP-OES, in LRM1 the content of Na is much larger. Also, TEM images (Figure 13) illustrate a layered structure with a d-spacing of 0.52 nm matching the 003 plane. This might be interpreted as a successful substitution of Na ions by Li^+ (Cao et al., 2020).

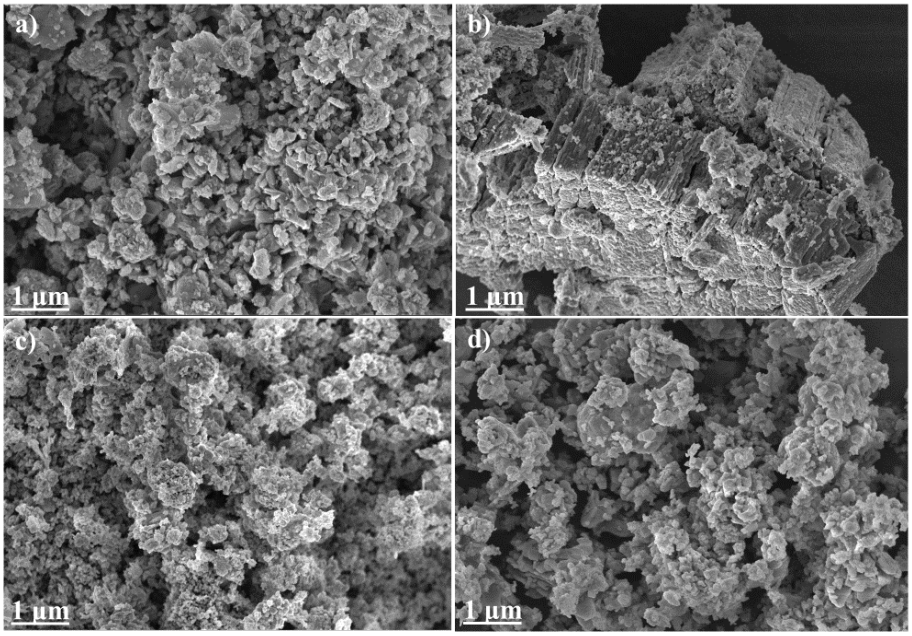

Figure 10. SEM images of a) Na precursor - LRM0, b) Na precursor - LRM1, c) Na precursor - LRM2, and d) Na precursor - LRM3, before ion exchange

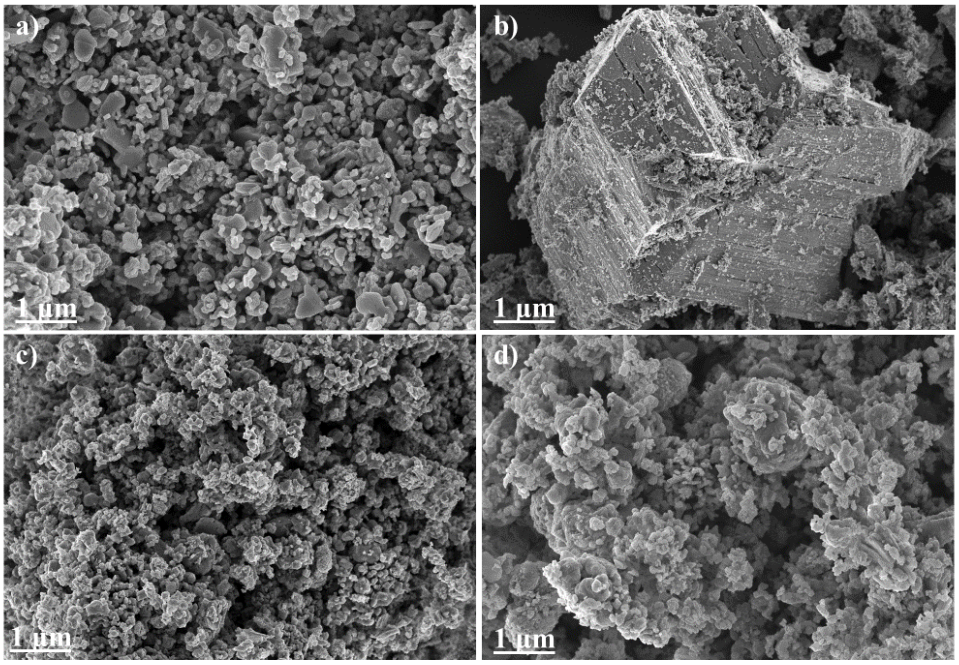

Figure 11. SEM images of a) LRM0, b) LRM1, c) LRM2, and d) LRM3 after ion exchange

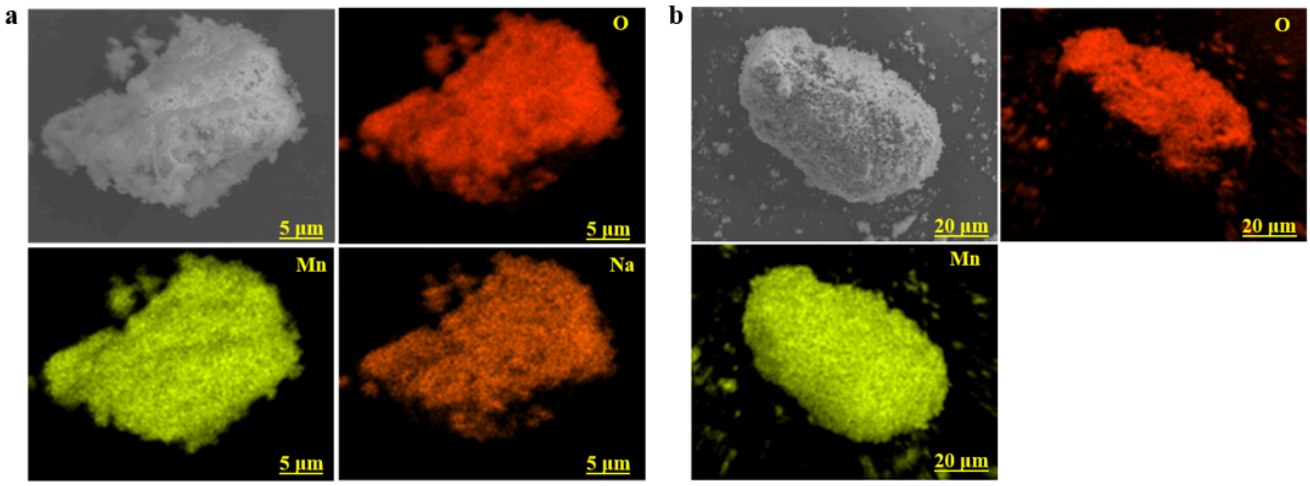

Figure 12. SEM-EDS elemental mapping of a) Na-precursor of LMR3 and b) LMR3

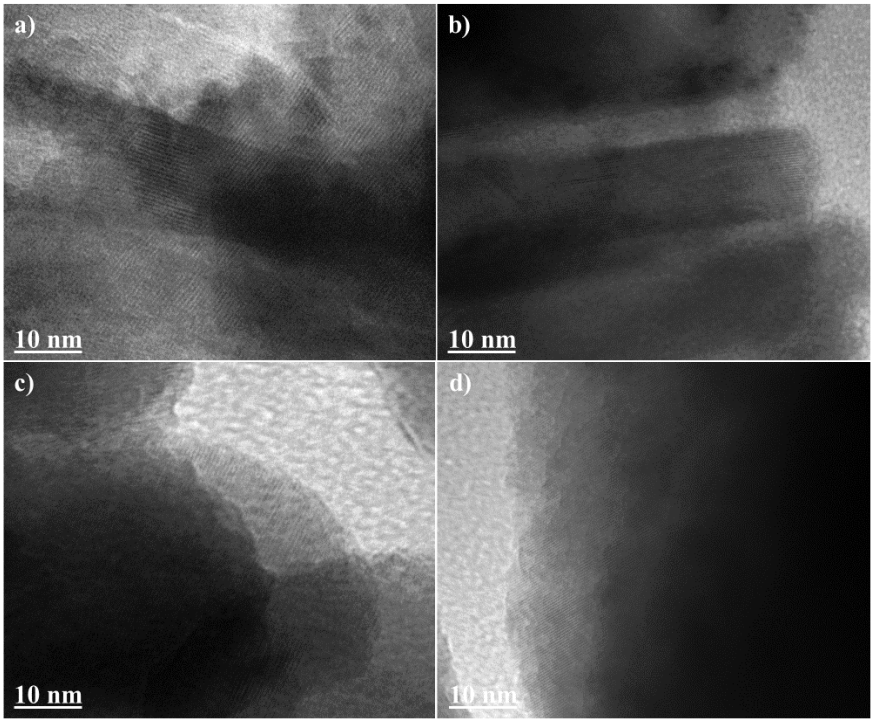

Figure 13. TEM images of a) LRM0, b) LRM1, c) LRM2, and d) LRM3

4.2. Electrochemical tests

When assessing cathode materials, the electrochemical test is an essential piece of evidence. Figure 14 demonstrates the results during five cycles and analogous dQ/dV curves are shown in Figure 16. How well samples performed electrochemically as a cathode material was determined using galvanostatic cycling. The LMR0, LMR1, LMR2, and LMR3 showed >50 mAh/g capacity on the initial charging. According to Figure 14, the beginning discharge capacities of LMR0, LMR1, LMR2, and LMR3 in the voltage range from 2V to 4.8V are 216 mAh/g, 165 mAh/g, 214 mAh/g, 190 mAh/g, respectively. Among these samples, LMR0 demonstrated the greatest capacity of 216 mAh/g, retaining 74.8% of its initial capacity. On the contrary, LMR1 exhibited an insufficient discharge capacity of 165 mAh/g but showed the best retention of capacity 89%, in particular specific capacity of 148 mAh/g after fifty cycles. The lower capacity might be assigned to the LRM1's specific surface area that is smaller than other samples. In addition, capacity retention for LRM2 and LRM3 are 72.7% and 77.5% respectively. Clearly the increasing capacity after the first cycle was detected in LRM2 and LRM3. One

explanation for this could be that ions of electrolytes have easier access to the AM's surface after the initial cycle.

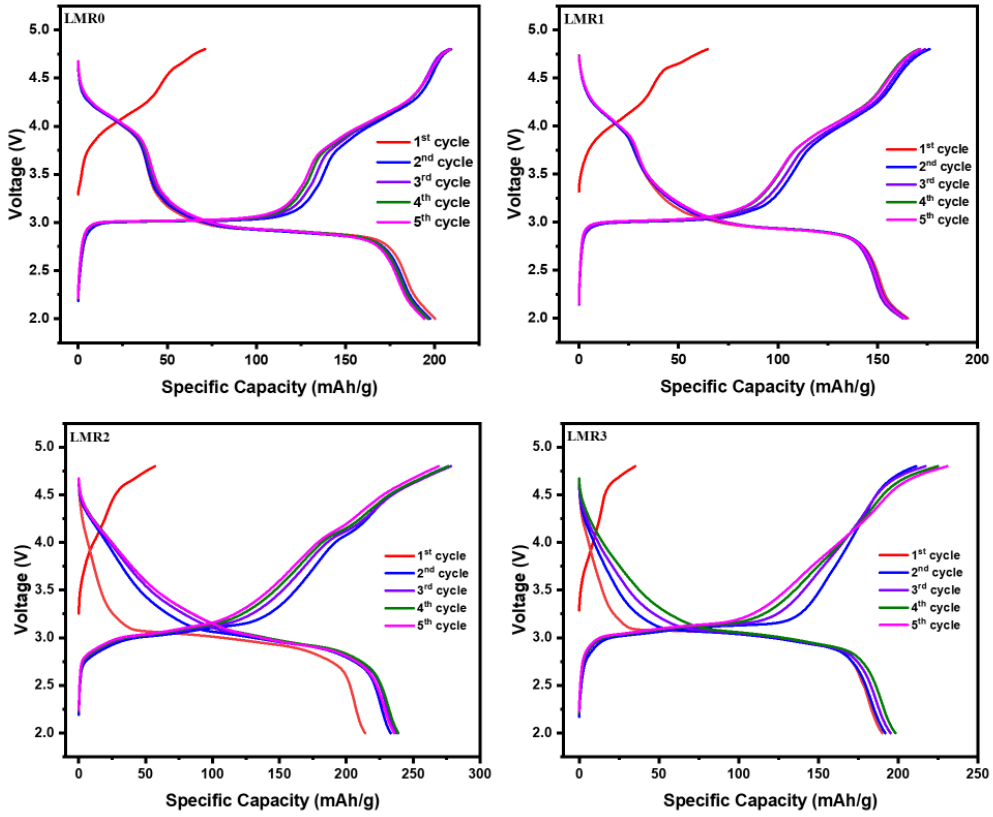

Figure 14. Charge and discharge curves of LMR0, LMR1, LMR2, and LMR3

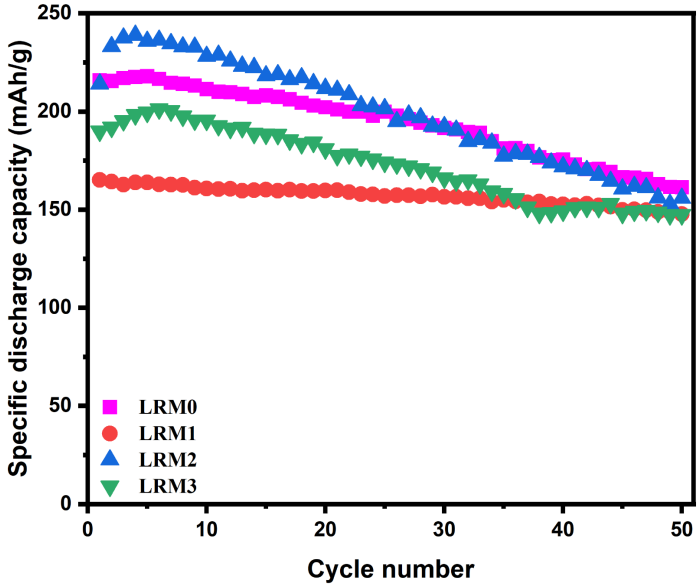

Figure 15. Cycle life of LMR0, LMR1, LMR2, and LMR3

The various Li^+ extraction procedures are related to the extensive area and plateau in the first charging phase (Li et al., 2018). From dQ/dV curves are clearly detected that each sample establishes small polarization, which is favorable for "ideal O redox" reported by Tsuchimoto et al. (2021). Two main reversible peaks of LMR2 and LMR3 are attributed to oxygen redox and Mn^{3+}/Mn^{4+} upon oxidation and reduction processes. As shown, the dQ/dV curves of LRM0 with LRM1 are similar. The first sharp redox peak occurs at 3.1 V on charge and the second at 2.9 V on discharge for both LRM0 and LRM1. According to Adamczyk & Pralong (2017): "Such redox potentials are consistent with the Mn^{4+}/Mn^{3+} couple." Unlike, the curves of LRM2 and LRM3 differ from above mentioned samples. LMR2 and LRM3 show similar two peaks between 2.7-4 V, except the peak in the range of 4-4.75 V. The broad peak at 4 V corresponds to Mn vacancy ordering. For this reason, it can be concluded that using Mn^{2+} and Mn^{3+}/Mn^{4+} precursors, synthesized in the same condition to obtain the same material with the same chemical formula, will still lead to different redox reactions.

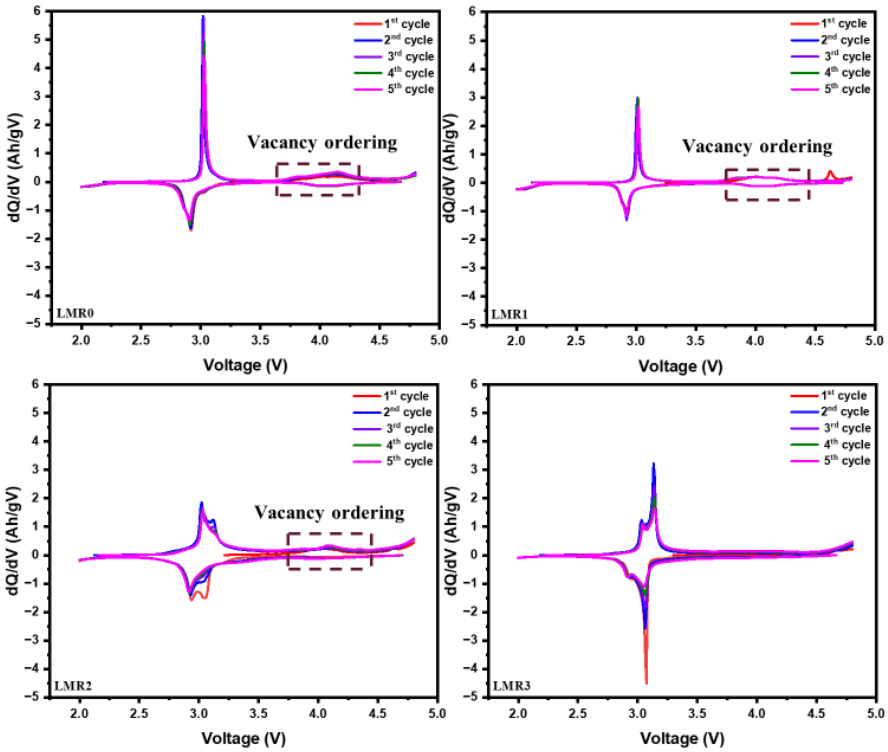

Figure 16. The dQ/dV curves of LMR0, LMR1, LMR2, and LMR3

The rate capability of the sample cathodes at various C rates is displayed in Figure 17. The target electrodes were checked at 0.1C, 0.5C, 1C, and 2C. Specific capacities of LRM1 at

studied C-rates were 143 mAh/g, 114 mAh/g, 95 mAh/g, 83 mAh/g, respectively and displayed the lowest capacity.

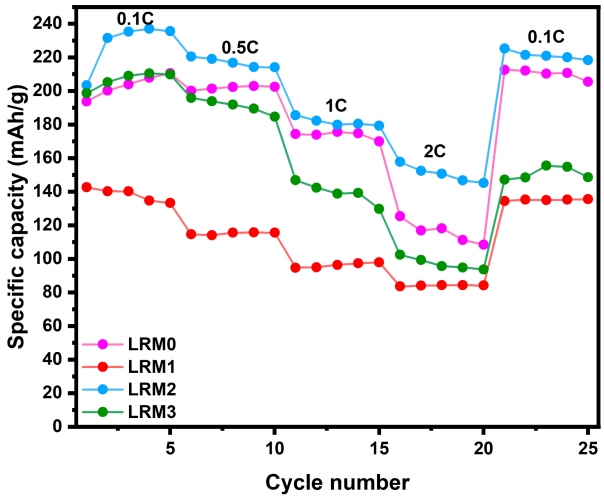

Figure 17. Rate capability of LMR0, LMR1, LMR2, and LMR3

Furthermore, EIS was used to study the electrochemical kinetics. Figure 18 shows the equivalent circuit that has been fitted. Xu et al. (2021) stated that "The semicircles in the Nyquist plots represent the resistance and capacitance of the electrolyte interface film of the cathode named the surface charge-transfer resistance (Rct)". Materials exhibit a similar profile on the Nyquist plot. It is argued that the higher Rct value is linked to the intricate creation process of cathode electrolyte interphase (CEI). The charge transfer resistance at the electrolyte interface and electrodes for the LRM0, LRM1, LRM2, and LRM3 are 73.5, 124, 106, and 86 Ohm, respectively.

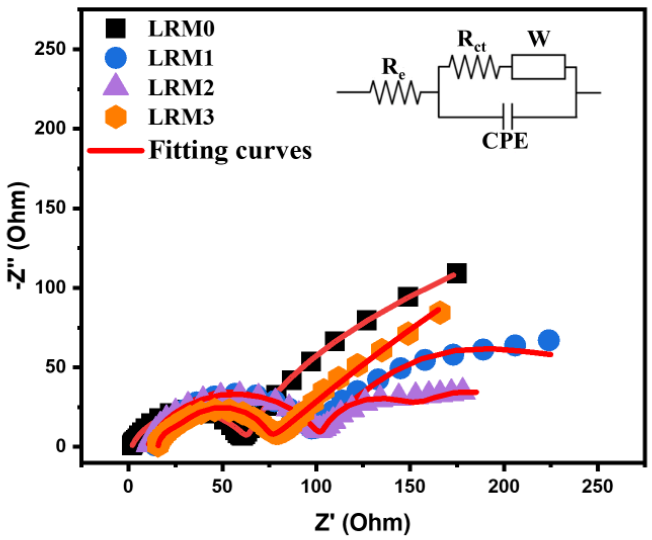

Figure 18. Nyquist plot of LMR0, LMR1, LMR2, and LMR3

4.3. Characterization method: Part II

Thermogravimetric analysis (TGA) and differential scanning calorimetry (DSC) were used to study the thermal behavior of the desired materials. The thermal behavior of LRM0, as determined by DSC and TGA analysis, is displayed in Figure 19. It is evident that mass loss began about 160 ◦C. The elimination of water might potentially be the cause of this. Molenda et al. reported that the changes of mass within the 300-820 ◦C temperature are linked with disappearance of cation vacancies and above this temperature oxygen vacancies diminishes. At high temperatures, Fd3m structure forms, and no obvious shift in weight after 850 ◦C related to obtaining the spinel phase (Berbenni et al., 2002)

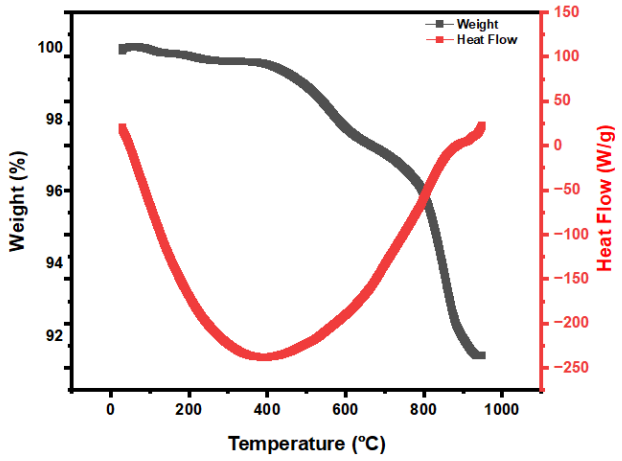

Figure 19. DSC and TGA thermograms of LRM0 cathode material

The relative abundance of pore size and specific surface area of samples were examined using nitrogen adsorption–desorption isotherms in order to learn more about the morphological features of the material. In accordance with IUPAC guidelines, the BET isotherms and the hysteresis loop seen for LRM0 were categorized as type IV. These results highlight the generated adsorbents' mesoporous properties. LRM0 had the following pore size distribution and specific surface area: 19.05 nm and 12.918 m^2/g. LRM1's surface area was detected as the smallest as it showed 2.0587 m^2/g, which was 6 times smaller compared to LRM0.

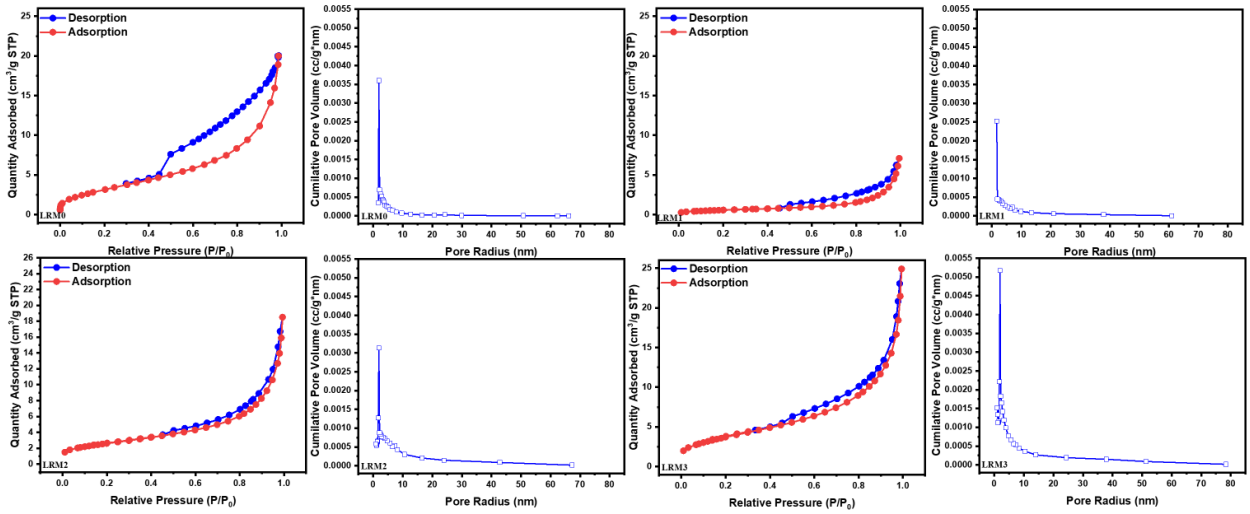

Figure 20. BET analysis of LRM0, LRM1, LRM2, and LRM3

The reversing and irreversing oxidation of oxygen-related behaviors occurring in LMR0 are further determined via in situ Raman spectroscopy. This approach is widely acknowledged as useful for precisely characterizing species related to oxygen (particularly peroxo species and O_2), which is advantageous for methodically deciphering the root causes of reversible/irreversible redox reactions happening in anion. Primarily, a clear reversible trend is observed in the peroxo stretching range (800–885 cm^{-1}) in the initial and subsequent cycles, suggesting that anion from the lattice might undergo oxidation to peroxo-related kinds upon charging and subsequent reduction to the starting condition following discharging. It is evident that the intensity of the stretch in the second cycle is higher than in the first one (Cao et al., 2021). To have a deeper knowledge in the formation of O-O peroxo pairs upon cycles DFT calculations are needed. It should be highlighted that a secondary reaction involving the electrolyte and active oxygen or superoxide anion that liberates from the lattice when it charges can account for the creation of Li_2CO_3.

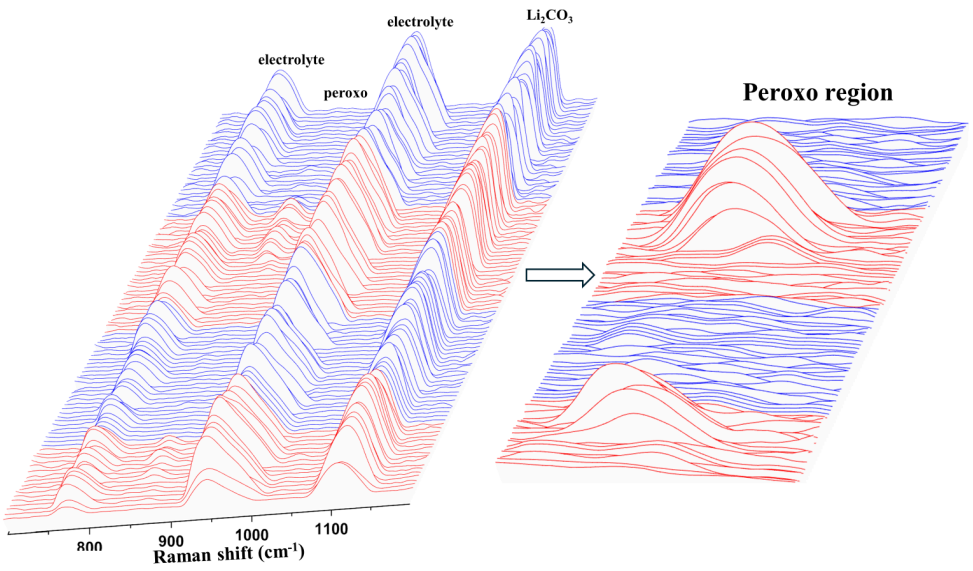

Figure 21. in situ Raman spectroscopy of first and second cycles of LRM0

Figure 22 displays the ex-situ XRD observations acquired after the first charge, charge-discharge, and OCV. The shrinkage and growth of lattice C, as well as the processes of delithiation and lithiation, are linked to the shifts in the (003) peak (Kim et al., 2023; Cao et al., 2022).

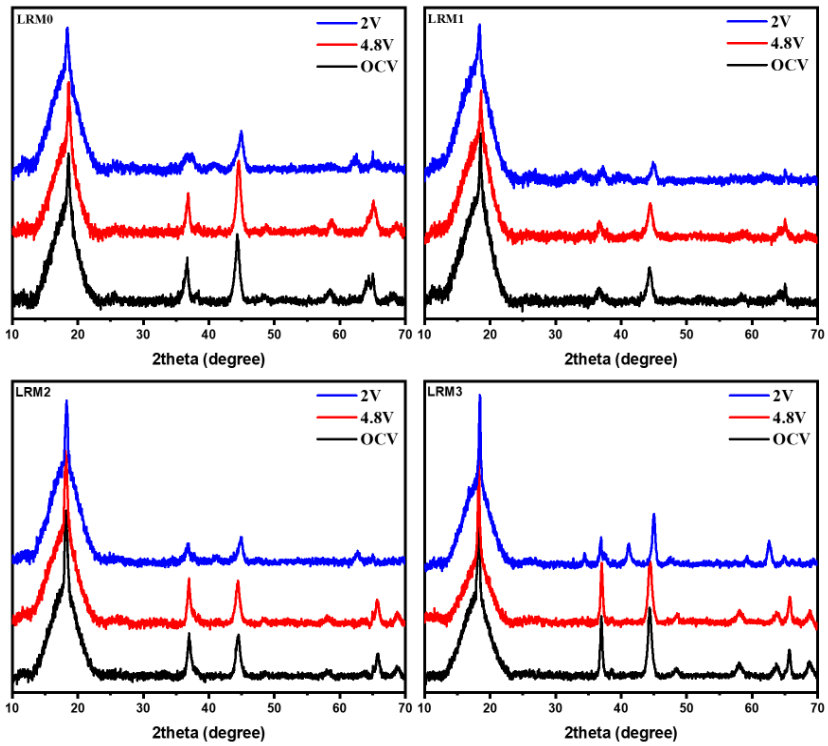

Figure 22. ex situ XRD pattern of LRM0, LRM1, LRM2, and LRM3

4.4. Spinel type LSP cathode material

After repeatedly heating at 700 ◦C, it can be seen that peaks became more crystalline and sharper. The XRD pattern corresponds to the spinel cubic Fd-3m space group reported by Siva et al. (2017). LSP consists of relatively regular faceleted particles with smooth surfaces and range in size from 300 to 400 nm on average (Figure 23). The particles of LSP are substantially smaller than those of LRM0 and LRM3. As mentioned beforehand, distinguishing the space group is challenging due to XRD patterns being similar. However, from the voltage profile, the changes in electrochemical performance are clearly detected. After 50 cycles, the LSP's initial discharge capacity of 218 mAh/g drops to about 100 mAh/g, showing severe capacity fading. It was argued that in spinel structure, Li ions are located in 8a tetrahedral sites while Mn in 16a octahedral ones (Siva et al., 2017).

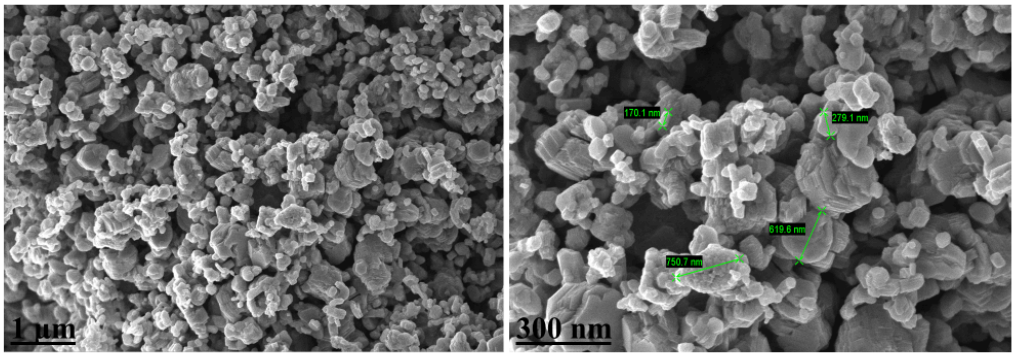

Figure 23. SEM images of LSP

There are two pairs of redox peaks in the 4V area, which indicate the two step (de)intercalation mechanism of Li^+ occurred at the 8a tetrahedral regions. ARedox peaks were seen in the 3 V region as a result of a switch in phase from cubic to tetragonal phases. Figure 23b represents the galvanostatic charge-discharge profiles at voltage range of 2-4.8V with current density of 20 mA/g. LSP showed irreversible phase transition reaction at 3.7-4V, which is seen from charge curves. The first discharge capacity is 218 mAh/g and specific capacity of about 75 mAh/g in the area of 3V. In the voltage window of 2-4.8V capacity retened completing 50 cycles is 50%. The capacity declined significantly after 11-12 cycles.

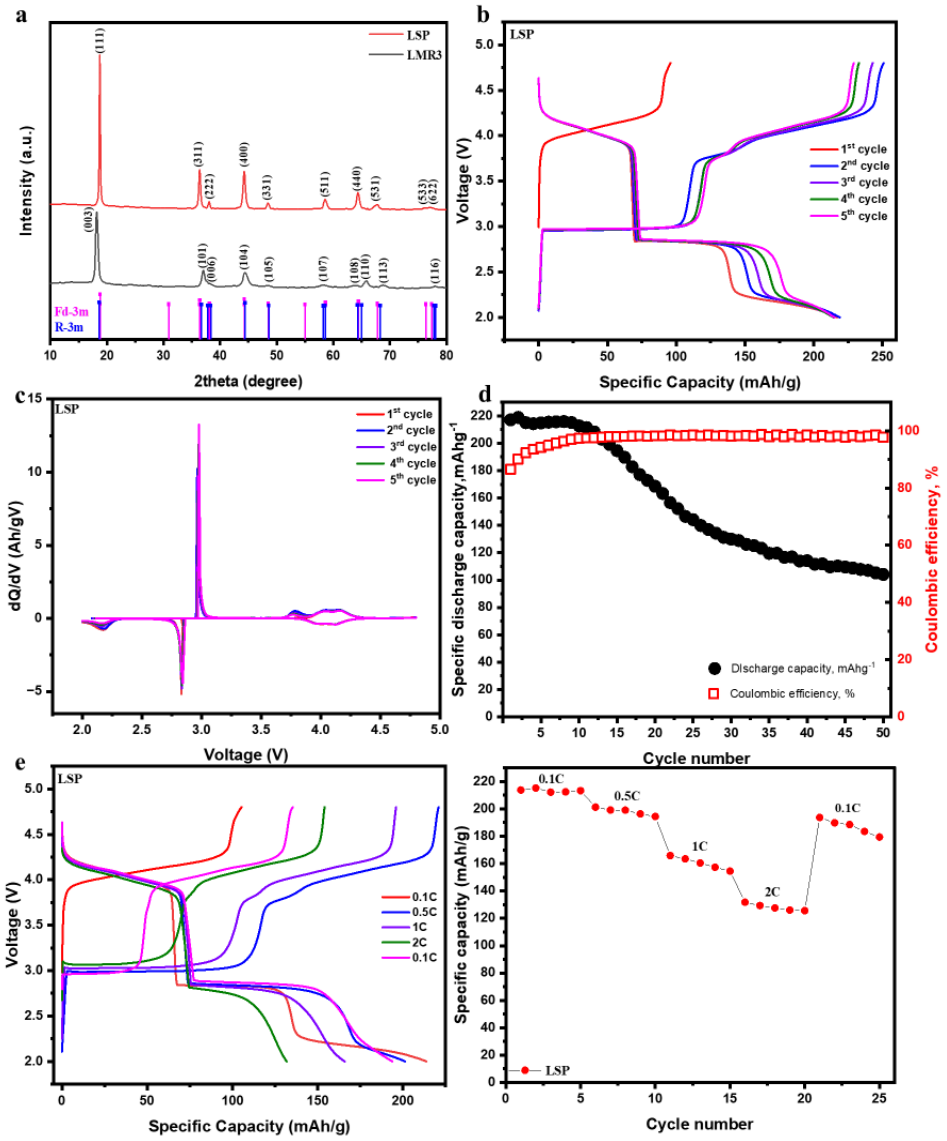

Figure 24. a) XRD pattern of LSP; b) charge-discharge curves; c) dQ/dV curves; d) cycle life; e) rate capability of LSP

Chapter 5. Conclusion

In conclusion, X-ray powder diffraction (XRD) is used to determine the crystal structure of $Li_2Mn_3O_7$. The synthesized $Li_2Mn_3O_7$'s XRD patterns are compatible with the R-3m phase, which aligns with earlier findings reported in the literature. Data from characterization techniques and electrochemical performance tests highlighted the variations amongst the samples under investigation, demonstrating the important role of starting precursors.

Important to note, precursor selection has an impact on the cathode material's purity, morphology, particle size, and crystallinity, all of which are directly related to the battery's capacity, stability, rate capability, and cyclability. From charge-discharge curves the differences in curves of LRM0/LRM1 and LRM2/LRM3 are detected as well as dQ/dV curves. The observable peaks of samples of Na precursor samples indicated the same triclinic phase with P1 space group, but differed in width, which could result in different numbers of vacancy ordering (Cao et al., 2021). Consequently, the vacancies play a crucial role in electrochemical performance. Among studied samples, LRM0 delivered a higher capacity of 216 mAh/g, and LRM1 the lowest with 165 mAh/g in the initial cycle. The capacity retention is 74.8% and 89%, respectively. The BET analysis showed that LRM1 exhibited the smallest surface area among samples, which might result in lowest specific capacity. The electrochemical behavior of Na-precursor samples emphasized varied charge-discharge and dQ/dV curves attributed to different reduction-oxidation reactions. To fully investigate the materials properties, in situ XRD, XPS, XAS, and high-resolution TEM analyses are needed.

References

Adamczyk, E., & B. Raveau. (2017). Na2Mn3O7: A Suitable Electrode Material for Na-Ion Batteries?. *Chemistry of Materials*, 29(11), 4645–4648. https://doi.org/10.1021/acs.chemmater.7b01390

Armstrong, A. R., Robertson, A. D., & Bruce, P. G. (2005). Overcharging manganese oxides: Extracting lithium beyond Mn4+. *Journal of Power Sources*, 146(1-2), 275–280. https://doi.org/10.1016/j.jpowsour.2005.03.104

Benoit, Shin ichi Nishimura, Watanabe, E., Lander, L., Akihisa Tsuchimoto, Jun Kikkawa, Kobayashi, E., Asakura, D., Okubo, M., & Yamada, A. (2018). Highly Reversible Oxygen‐Redox Chemistry at 4.1 V in Na4/7−x[□1/7Mn6/7]O2 (□: Mn Vacancy). *Advanced Energy Materials*, 8(20). https://doi.org/10.1002/aenm.201800409

Berbenni, V., & Marini, A. (2002). Thermoanalytical (TGA-DSC) and high temperature X-ray diffraction (HT-XRD) study of the thermal decomposition processes in Li2CO3–MnO mixtures. *Journal of Analytical and Applied Pyrolysis*, 64(1), 43–58. https://doi.org/10.1016/s0165-2370(01)00169-3

Bonani Seteni, Nomasonto Rapulenyane, Jane Catherine Ngila, Siyasanga Mpelane, & Luo, H. (2017). Coating effect of LiFePO 4 and Al 2 O 3 on Li 1.2 Mn 0.54 Ni 0.13 Co 0.13 O 2 cathode surface for lithium ion batteries. *Journal of Power Sources*, 353, 210–220. https://doi.org/10.1016/j.jpowsour.2017.04.008

Cao, X., Li, H., Qiao, Y., Jia, M., Li, X., Cabana, J., & Zhou, H. (2020). Stabilizing Anionic Redox Chemistry in a Mn‐Based Layered Oxide Cathode Constructed by Li‐Deficient Pristine State. *Advanced Materials*, 33(2). https://doi.org/10.1002/adma.202004280

Cao, X., Qiao, Y., Jia, M., He, P., & Zhou, H. (2021). Ion‐Exchange: A Promising Strategy to Design Li‐Rich and Li‐Excess Layered Cathode Materials for Li‐Ion Batteries. *Advanced Energy Materials*, 12(4), 2003972. https://doi.org/10.1002/aenm.202003972

Cao, X., Li, H., Qiao, Y., He, P., Qian, Y., Yue, X., Jia, M., Cabana, J., & Zhou, H. (2022). Reversible anionic redox chemistry in layered Li4/7[□1/7Mn6/7]O2 enabled by stable Li–O-vacancy configuration. *Joule*, 6(6), 1290–1303. https://doi.org/10.1016/j.joule.2022.05.006

Croy, J. E., Balasubramanian, M., Gallagher, K. P., & Burrell, A. K. (2015). Review of the U.S. Department of Energy's "Deep Dive" Effort to Understand Voltage Fade in Li- and Mn-Rich Cathodes. *Accounts of Chemical Research*, 48(11), 2813–2821. https://doi.org/10.1021/acs.accounts.5b00277

Chen, S., Tao, R., Guo, C., Zhang, W., Liu, X., Yang, G., Guo, P., Sun, G., Liang, J., & Lu, S.-Y. (2021). A new trick for an old technology: Ion exchange syntheses of advanced energy storage and conversion nanomaterials. *Energy Storage Materials*, 41, 758–790. https://doi.org/10.1016/j.ensm.2021.06.043

Dunn, B., Kamath, H., & Tarascon, J. (2011). Electrical energy storage for the grid: A battery of choices. *Science*, 334(6058), 928-935. https://doi.org/10.1126/science.1212741

Fischer, D., Hoppe, R., W. Schäfer, & Knight, K. S. (1993). Koordinationszahl 4 oder 6 für Lithium??: Die Kristallstruktur von wasserfreiem Lithiumpermanganat, Li[MnO4]. *Zeitschrift Für Anorganische Und Allgemeine Chemie*, 619(8), 1419–1425. https://doi.org/10.1002/zaac.19936190817

Gent, W. E., Lim, K., Liang, Y., Li, Q., Barnes, T. A., Ahn, S., Stone, K. H., McIntire, M., Hong, J., Song, J.-H., Li, Y., Mehta, A., Stefano Ermon, Tolek Tyliszczak, Kilcoyne, D., Vine, D., Jin Bae

Park, Doo, S.-K., Toney, M. F., & Yang, W. (2017). Coupling between oxygen redox and cation migration explains unusual electrochemistry in lithium-rich layered oxides. 8(1). https://doi.org/10.1038/s41467-017-02041-x

Gu, M., Belharouak, I., Zheng, J., Wu, H., Xiao, J., Genc, A., Amine, K., Thevuthasan, S., Baer, D. R., Zhang, J.-G., Browning, N. D., Liu, J., & Wang, C. (2012). Formation of the Spinel Phase in the Layered Composite Cathode Used in Li-Ion Batteries. *ACS Nano*, 7(1), 760–767. https://doi.org/10.1021/nn305065u

Gwon, H., Kim, S.-W., Park, Y.-U., Hong, J., Ceder, G., Jeon, S., & Kang, K. (2014). Ion-Exchange Mechanism of Layered Transition-Metal Oxides: Case Study of LiNi0.5Mn0.5O2. *Inorganic Chemistry*, 53(15), 8083–8087. https://doi.org/10.1021/ic501069x

Hu, E., Yu, X., Lin, R., Bi, X., Lu, J., Bak, S.-M., Nam, K.-W., Xin, H. L., Jaye, C., Fischer, D. A., Amine, K., & Yang, X.-Q. (2018). Evolution of redox couples in Li- and Mn-rich cathode materials and mitigation of voltage fade by reducing oxygen release. 3(8), 690–698. https://doi.org/10.1038/s41560-018-0207-z

Hy, S., Felix, F., Rick, J., Su, W.-N., & Hwang, B.-J. (2014). Direct In situ Observation of Li2O Evolution on Li-Rich High-Capacity Cathode Material, Li[NixLi(1–2x)/3Mn(2–x)/3]O2 ($0 \leq x \leq 0.5$). 136(3), 999–1007. https://doi.org/10.1021/ja410137s

Jiang, M., Key, B., Ying Shirley Meng, & Grey, C. P. (2009). Electrochemical and Structural Study of the Layered, "Li-Excess" Lithium-Ion Battery Electrode Material Li[Li1/9Ni1/3Mn5/9]O2. 21(13), 2733–2745. https://doi.org/10.1021/cm900279u

Kim, T., Ono, L. K., & Qi, Y. (2023). Understanding the active formation of a cathode–electrolyte interphase (CEI) layer with energy level band bending for lithium-ion batteries. *Journal of Materials Chemistry A*, 11(1), 221–231. https://doi.org/10.1039/d2ta07565b

Koga, H., Croguennec, L., Ménétrier, M., Kaïs Douhil, Belin, S., Bourgeois, L., Emmanuelle Suard, Weill, F., & Delmas, C. (2013). Reversible Oxygen Participation to the Redox Processes Revealed for Li1.20Mn0.54Co0.13Ni0.13O2. *Journal of the Electrochemical Society*, 160(6), A786–A792. https://doi.org/10.1149/2.038306jes

Koga, H., Croguennec, L., Ménétrier, M., Philippe Mannessiez, Weill, F., Delmas, C., & Belin, S. (2014). Operando X-ray Absorption Study of the Redox Processes Involved upon Cycling of the Li-Rich Layered Oxide Li1.20Mn0.54Co0.13Ni0.13O2 in Li-Ion Batteries. *Journal of Physical Chemistry C*, 118(11), 5700–5709. https://doi.org/10.1021/jp412197z

Lee, E., Koritala, R. E., Miller, D. J., & Johnson, C. (2014). Aluminum and Gallium Substitution into 0.5Li2MnO3·0.5Li(Ni0.375Mn0.375Co0.25)O2 Layered Composite and the Voltage Fade Effect. *Journal of the Electrochemical Society*, 162(3), A322–A329. https://doi.org/10.1149/2.0321503jes

Lee, W., Muhammad, S., Sergey, C., Lee, H., Yoon, J., Kang, Y., & Yoon, W. (2020). Advances in the Cathode Materials for Lithium Rechargeable Batteries. *Angewandte Chemie International Edition*, *59*(7), 2578–2605. https://doi.org/10.1002/anie.201902359

Li, M., Lu, J., Chen, Z., & Amine, K. (2018). 30 Years of Lithium-Ion Batteries. *Advanced Materials*, *30*(33), 1800561. https://doi.org/10.1002/adma.201800561

Li, X., Qiao, Y., Guo, S., Xu, Z., Zhu, H., Zhang, X., Yang, Y., He, P., Ishida, M., & Zhou, H. (2018). Direct Visualization of the Reversible O2− /O− Redox Process in Li-Rich Cathode Materials. *Advanced Materials*, 30(14), 1705197–1705197. https://doi.org/10.1002/adma.201705197

Li, X., Qiao, Y., Guo, S., Xu, Z., Zhu, H., Zhang, X., Yang, Y., He, P., Ishida, M., & Zhou, H. (2018). Direct Visualization of the Reversible O2− /O− Redox Process in Li-Rich Cathode Materials. *Advanced Materials*, 30(14), 1705197–1705197. https://doi.org/10.1002/adma.201705197

Liu, H., Harris, K. J., Jiang, M., Wu, Y., Goward, G. R., & Botton, G. A. (2018). Unraveling the Rapid Performance Decay of Layered High-Energy Cathodes: From Nanoscale Degradation to Drastic Bulk Evolution. *ACS Nano*, 12(3), 2708–2718. https://doi.org/10.1021/acsnano.7b08945

Lu, Z., Chen, Z., & Dahn, J. R. (2003). Lack of Cation Clustering in Li[NixLi1/3-2x/3Mn2/3-x/3]O2 ($0 < x \leq 1/2$) and Li[CrxLi(1-x)/3Mn(2-2x)/3]O2 ($0 < x < 1$). *Chemistry of Materials*, 15(16), 3214–3220. https://doi.org/10.1021/cm030194s

Lu, Z., Beaulieu, L. Y., Donaberger, R. A., Thomas, C. L., & Dahn, J. R. (2002). Synthesis, Structure, and Electrochemical Behavior of Li[Ni[sub x]Li[sub 1/3−2x/3]Mn[sub 2/3−x/3]]O[sub 2]. *Journal of the Electrochemical Society*, 149(6), A778. https://doi.org/10.1149/1.1471541

Luo, K., Roberts, M., Hao, R., Guerrini, N., Pickup, D. M., Liu, Y.-S., Edström, K., Guo, J., Chadwick, A. V., Duda, L.-C., & Bruce, P. G. (2016). Charge-compensation in 3d-transition-metal-oxide intercalation cathodes through the generation of localized electron holes on oxygen. *Nature Chemistry*, 8(7), 684–691. https://doi.org/10.1038/nchem.2471

Luo, Y., Pan, Q., Wei, H., Huang, Y., Tang, L., Wang, Z., Yan, C., Mao, J., Dai, K., Wu, Q., Zhang, X., & Zheng, J. (2023). Fundamentals of Ion‐Exchange Synthesis and Its Implications in Layered Oxide Cathodes: Recent Advances and Perspective. *Advanced Energy Materials*, 13(21). https://doi.org/10.1002/aenm.202300125

Manthiram, A. (2017). An Outlook on Lithium Ion Battery Technology. *ACS Central Science*, 3(10), 1063–1069. https://doi.org/10.1021/acscentsci.7b00288

Molenda, M., R. Dziembaj, E. Podstawka, & L.M. Proniewicz. (2005). Changes in local structure of lithium manganese spinels (Li:Mn=1:2) characterised by XRD, DSC, TGA, IR, and Raman spectroscopy. *Journal of Physics and Chemistry of Solids*, 66(10), 1761–1768. https://doi.org/10.1016/j.jpcs.2005.09.001

Qing, R., Shi, J., Xiao, D., Zhang, X., Yin, Y., Zhai, Y., Gu, L., & Guo, Y. (2015). Enhancing the Kinetics of Li‐Rich Cathode Materials through the Pinning Effects of Gradient Surface Na+ Doping. *Advanced Energy Materials*, 6(6). https://doi.org/10.1002/aenm.201501914

Radin, M. D., Vinckeviciute, J., Seshadri, R., & Van der Ven, A. (2019). Manganese oxidation as the origin of the anomalous capacity of Mn-containing Li-excess cathode materials. *Nature Energy*, 4(8), 639–646. https://doi.org/10.1038/s41560-019-0439-6

Raekelboom, E. A., Hector, A. L., Owen, J. R., Ģirts Vītiņš, & Weller, M. T. (2001). Syntheses, Structures, and Preliminary Electrochemistry of the Layered Lithium and Sodium Manganese(IV) Oxides, A2Mn3O7. *Chemistry of Materials*, 13(12), 4618–4623. https://doi.org/10.1021/cm011105j

Robertson, A. D., & Bruce, P. G. (2002). The origin of electrochemical activity in Li2MnO3. *Chemical Communications*, 23, 2790–2791. https://doi.org/10.1039/b207945c

Sathiya, M., Abakumov, A. M., Foix, D., Rousse, G., Ramesha, K., Saubanère, M., Doublet, M. L., Vezin, H., Laisa, C. P., Prakash, A. S., Gonbeau, D., VanTendeloo, G., & Tarascon, J-M. (2014). Origin of voltage decay in high-capacity layered oxide electrodes. *Nature Materials*, 14(2), 230–238. https://doi.org/10.1038/nmat4137

Seo, D.-H., Lee, J., Urban, A., Malik, R., Kang, S., & Ceder, G. (2016). The structural and chemical origin of the oxygen redox activity in layered and cation-disordered Li-excess cathode materials. *Nature Chemistry*, 8(7), 692–697. https://doi.org/10.1038/nchem.2524

Siva Reddy Kasireddy, Binitha Gangaja, Nair, S. V., & Dhamodaran Santhanagopalan. (2017). Mn 4+ rich surface enabled elevated temperature and full-cell cycling performance of LiMn 2 O 4 cathode material. *Electrochimica Acta*, 250, 359–367. https://doi.org/10.1016/j.electacta.2017.08.054

Thackeray, M. M. (1997). Manganese oxides for lithium batteries. *Progress in Solid State Chemistry*, 25(1-2), 1–71. https://doi.org/10.1016/s0079-6786(97)81003-5

Thackeray, M. M., Kang, S.-H., Johnson, C. S., Vaughey, J. T., Benedek, R., & Hackney, S. A. (2007). Li2MnO3-stabilized LiMO2 (M = Mn, Ni, Co) electrodes for lithium-ion batteries. *Journal of Materials Chemistry*, 17(30), 3112. https://doi.org/10.1039/b702425h

Tsuchimoto, A., Shi, X.-M., Kawai, K., Mortemard de Boisse, B., Kikkawa, J., Asakura, D., Okubo, M., & Yamada, A. (2021). Nonpolarizing oxygen-redox capacity without O-O dimerization in Na2Mn3O7. *Nature Communications*, 12(1), 631. https://doi.org/10.1038/s41467-020-20643-w

Wang, J., He, X., Elie Paillard, Laszczynski, N., Li, J., & Khademhosseini, A. (2016). Lithium- and Manganese-Rich Oxide Cathode Materials for High-Energy Lithium Ion Batteries. 6(21), 1600906–1600906. https://doi.org/10.1002/aenm.201600906

Xu, B., Fell, C. R., Chi, M., & Meng, Y. S. (2011). Identifying surface structural changes in layered Li-excess nickel manganese oxides in high voltage lithium ion batteries: A joint experimental and theoretical study. *Energy & Environmental Science*, 4(6), 2223. https://doi.org/10.1039/c1ee01131f

Xu, W., Zheng, Y., Lin, L., Lei, W., Wang, Z., Song, H., Cheng, Y., Qi, R., Peng, H., Lin, H., Yang, Z., & Huang, R. (2021). Atomic insights into surface orientations and oxygen vacancies in the LiMn2O4 cathode for lithium storage. *Journal of Alloys and Compounds*, 870, 159387–159387. https://doi.org/10.1016/j.jallcom.2021.159387

Xue, Z., Guan, D., Zeng, J., Cao, Y., Peng, Z., Hu, G., & Du, K. (2023). Research on the assembly process of full coin cells: key factors affecting data reliability. *Ionics*, 29(12), 5285–5293. https://doi.org/10.1007/s11581-023-05225-2

Yuan, M., Liu, H., & Ran, F. (2023). Fast-charging cathode materials for lithium & sodium ion batteries. *Materials Today.* https://doi.org/10.1016/j.mattod.2023.02.007

Yin, W., Grimaud, A., Rousse, G., Abakumov, A. M., Anatoliy Senyshyn, Zhang, L., Sigita Trabesinger, Antonella Iadecola, Foix, D., Domitille Giaume, & Jean‐Marie Tarascon. (2020). Structural evolution at the oxidative and reductive limits in the first electrochemical cycle of Li1.2Ni0.13Mn0.54Co0.13O2. *Nature Communications*, 11(1). https://doi.org/10.1038/s41467-020-14927-4

Zheng, J., Xu, P., Gu, M., Xiao, J., Browning, N. D., Yan, P., Wang, C., & Zhang, J.-G. (2015). Structural and Chemical Evolution of Li- and Mn-Rich Layered Cathode Material. *Chemistry of Materials*, 27(4), 1381–1390. https://doi.org/10.1021/cm5045978

Zubi, G., Dufo-López, R., Carvalho, M., & Pasaoglu, G. (2018). The lithium-ion battery: State of the art and future perspectives. *Renewable and Sustainable Energy Reviews*, 89, 292–308. https://doi.org/10.1016/j.rser.2018.03.002

Appendices

Appendix A

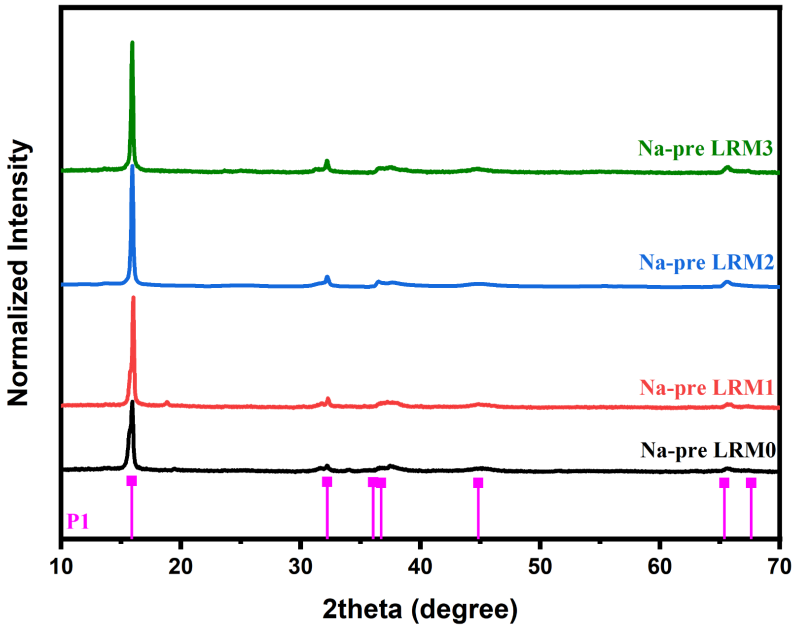

Figure A.1. XRD pattern of Na-precursor samples

Appendix B

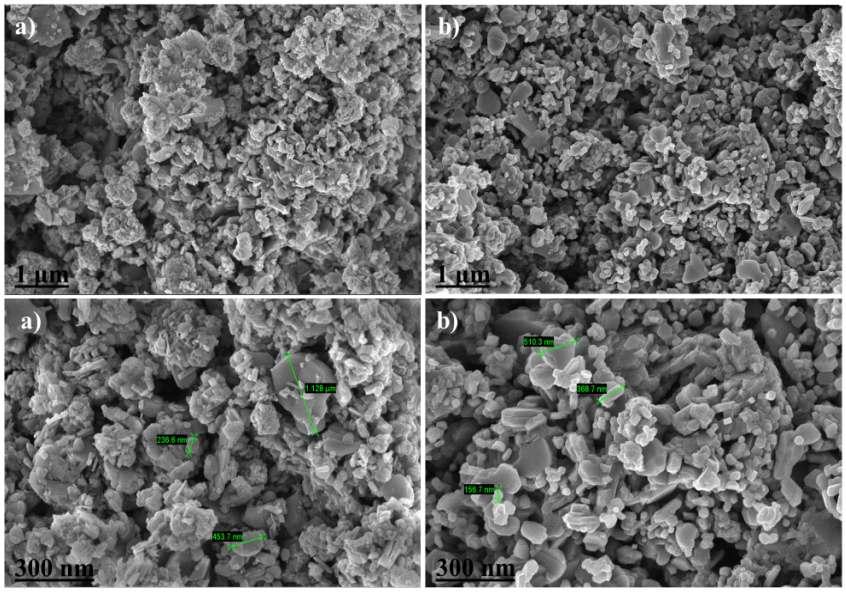

Figure B.1. SEM images of LRM0 a) before ion exchange and b) after

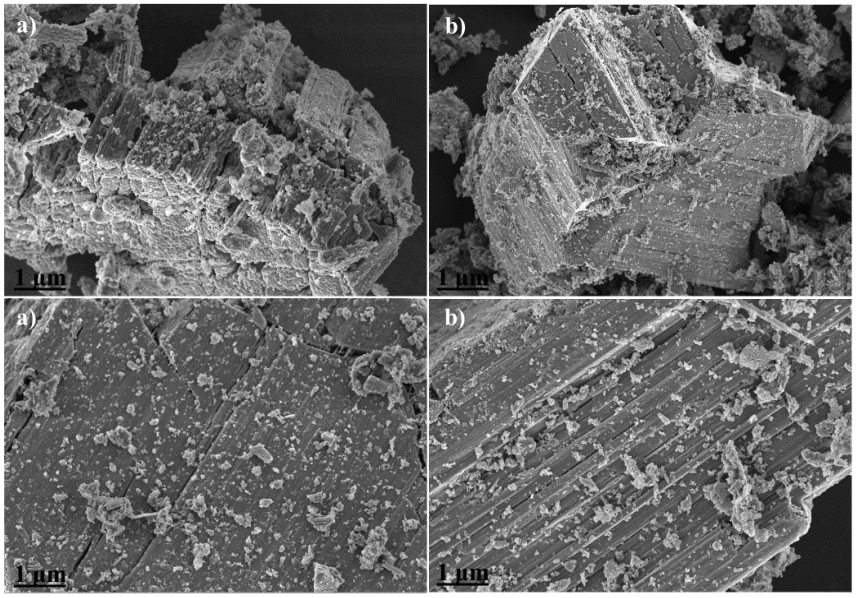

Figure B.2. SEM images of LRM1 a) before ion exchange and b) after

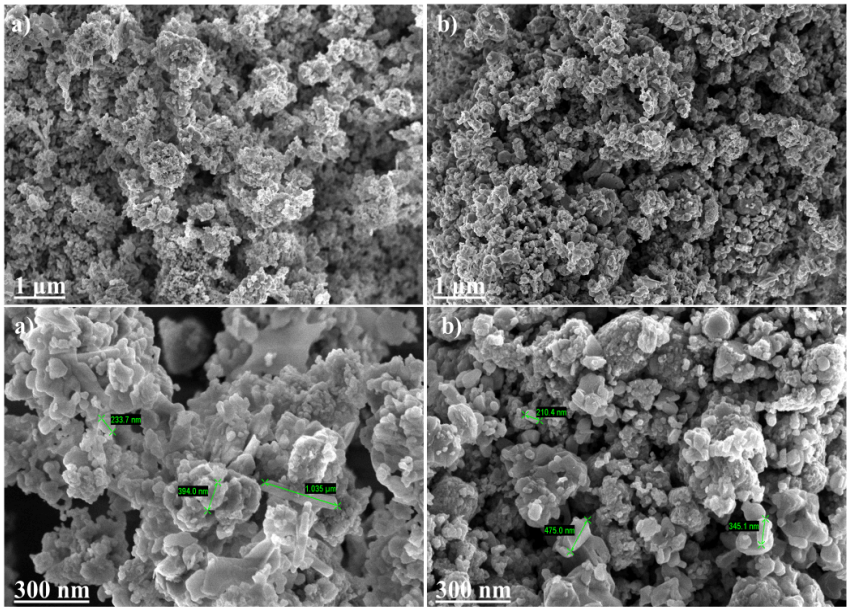

Figure B.3. SEM images of LRM2 a) before ion exchange and b) after

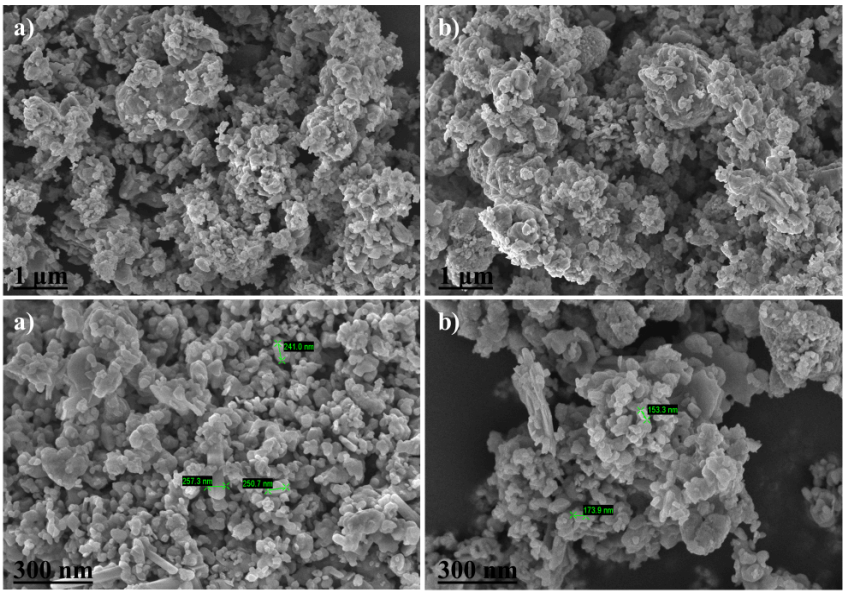

Figure B.4. SEM images of LRM3 a) before ion exchange and b) after

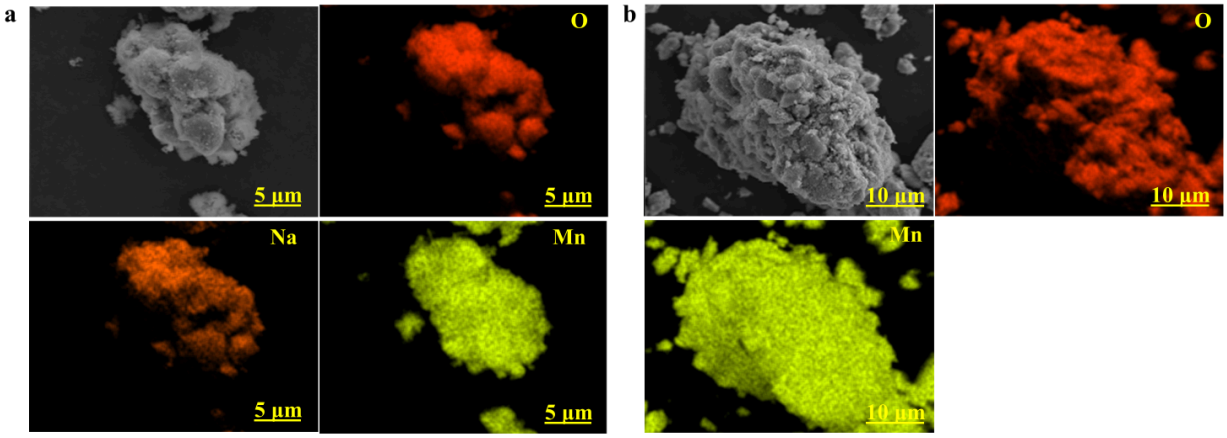

Element	Line	Mass%	Atom%
C	K	56.72±0.02	69.94±0.03
O	K	26.77±0.03	24.78±0.03
Na	K	3.07±0.01	1.98±0.01
Mn	K	11.22±0.02	3.02±0.00
Au	M	1.62±0.01	0.12±0.00
Total		100.00	100.00

Element	Line	Mass%	Atom%
C	K	35.79±0.02	51.52±0.03
O	K	37.27±0.03	40.27±0.03
Mn	K	25.10±0.02	7.90±0.01
Au	M	1.19±0.01	0.10±0.00
Total		100.00	100.00

Figure B.5. SEM-EDS of LRM0

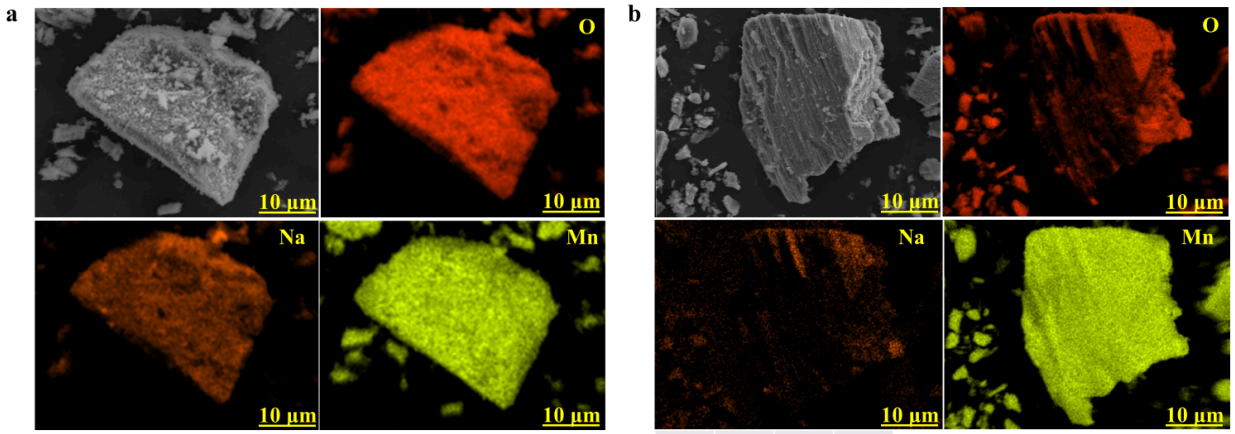

Element	Line	Mass%	Atom%
C	K	33.74±0.02	47.46±0.03
O	K	38.04±0.03	40.17±0.03
Na	K	9.39±0.02	6.90±0.01
Mn	K	17.38±0.02	5.35±0.01
Au	M	1.44±0.01	0.12±0.00
Total		100.00	100.00

Element	Line	Mass%	Atom%
C	K	42.30±0.02	59.62±0.03
O	K	30.52±0.03	32.30±0.03
Na	K	0.26±0.00	0.19±0.00
Mn	K	24.61±0.03	7.58±0.01
Au	M	1.71±0.01	0.15±0.00
Total		100.00	100.00

Figure B.6. SEM-EDS of LRM1

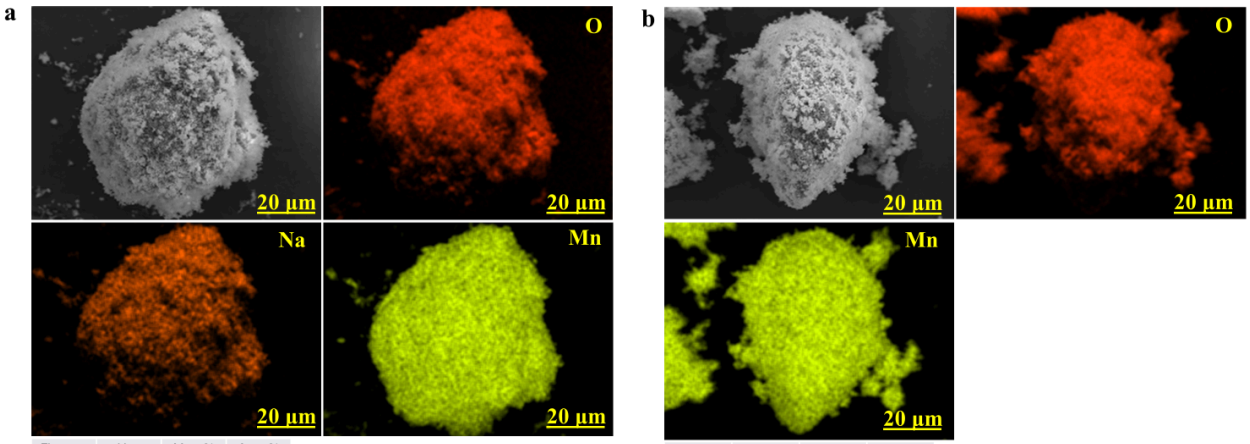

Element	Line	Mass%	Atom%
C	K	48.37±0.02	62.45±0.02
O	K	32.00±0.03	31.02±0.03
Na	K	3.27±0.01	2.20±0.01
Mn	K	14.50±0.02	4.09±0.00
Au	M	1.34±0.01	0.11±0.00
Total		100.00	100.00

Element	Line	Mass%	Atom%
C	K	42.47±0.02	56.69±0.02
O	K	37.75±0.03	37.82±0.03
Mn	K	17.93±0.02	5.23±0.01
Au	M	1.25±0.01	0.10±0.00
Total		100.00	100.00

Figure B.7. SEM-EDS of LRM2

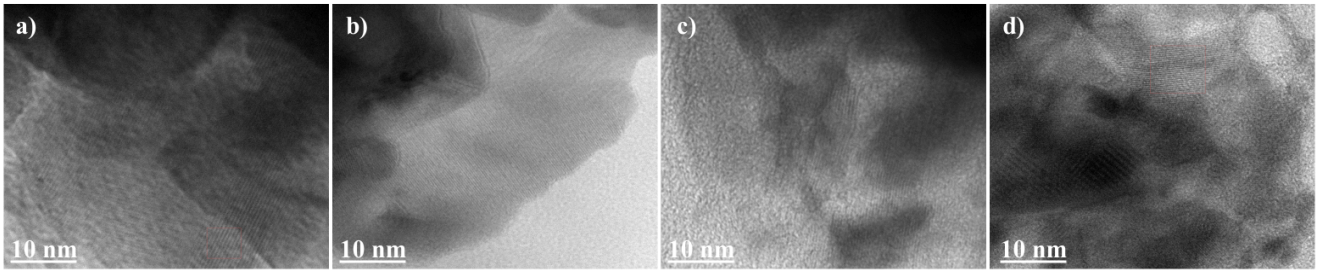

Figure B.8. TEM images of Na-precursor a) LRM0, b) LRM1, c) LRM2, and d) LRM3

Appendix C

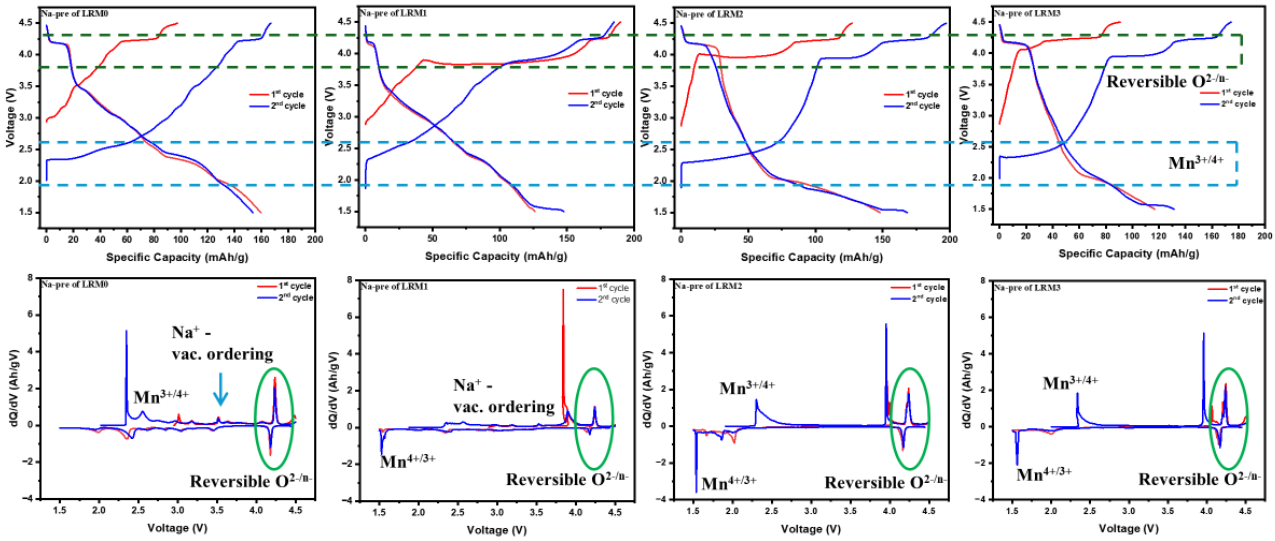

Figure C.1. Charge-discharge curves and dQ/dV curves of Na-precursors of a) LMR0, b) LMR2, and c) LMR3

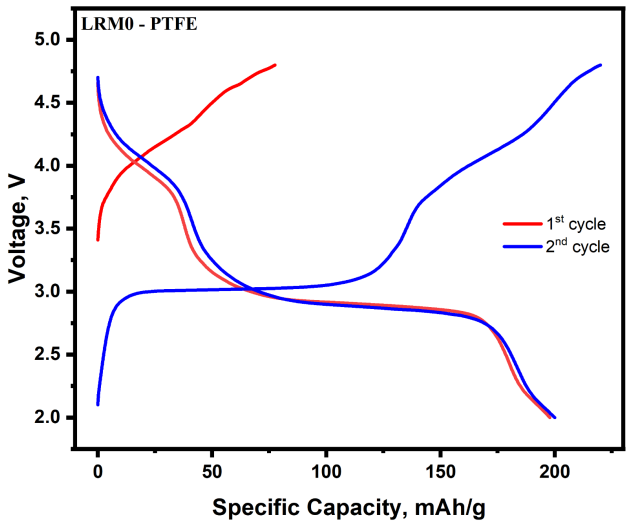

Figure C.2. Charge-discharge curves of LRM0, the slurry was prepared by mixing 70% AM, 20% carbon black and 10% PTFE

Appendix D

Table D.2. Charge transfer resistance values of samples

Sample name	R1 (Ohm)	R2 (Ohm)
LRM0	1.9	73.56
LRM1	14	124.94
LRM2	10.9	106.72
LRM3	15.94	86.90

Appendix E

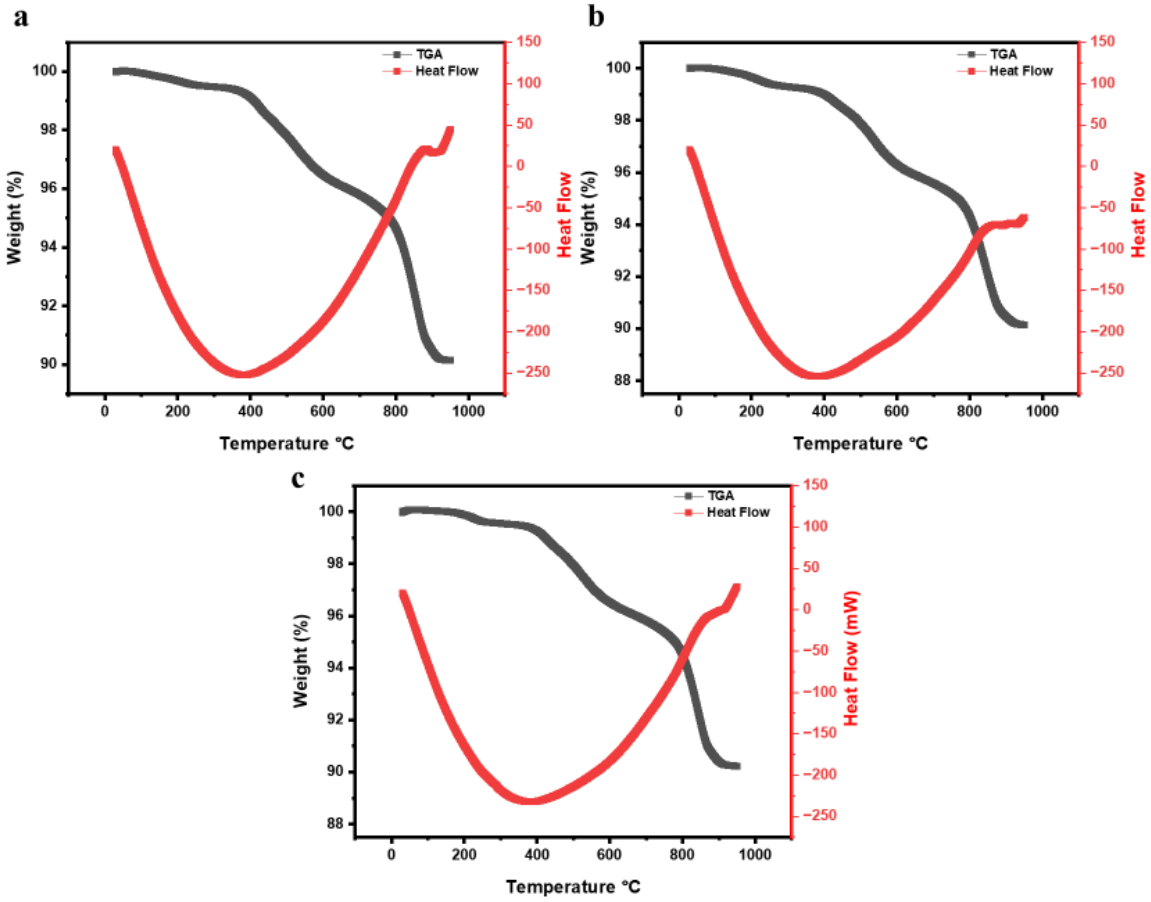

Figure E.1. DSC and TGA thermograms of LMR1, LMR2, and LMR3 cathode materials